MECHANICAL BEHAVIOR OF GRANULAR MATERIALS REINFORCED BY DISPOSABLE FACE-MASK CHIPS

NA YANG

PhD

The Hong Kong Polytechnic University

2024

The Hong Kong Polytechnic University

Department of Civil and Environmental Engineering

Mechanical Behavior of Granular Materials Reinforced by Disposable Face-mask Chips

Na Yang

A thesis submitted in partial fulfilment of the requirements for the degree of

Doctor of Philosophy

January 2024

CERTIFICATE OF ORIGINALITY

I hereby declare that this thesis is my own work and that, to the best of my knowledge and belief, it reproduces no material previously published or written, nor material that has been accepted for the award of any other degree of diploma, except where due acknowledgement has been made in the text.

Signature:

Name: NA YANG

Abstract of thesis entitled

MECHANICAL BEHAVIOR OF GRANULAR MATERIALS REINFORCED BY DISPOSABLE FACE-MASK CHIPS

Recently, there has been a growing interest in utilizing disposable face masks as a reinforcing additive to enhance the engineering performance of granular soils. This thesis investigates the mechanical behavior of face mask chips-sand mixture (MSM) from experiments to constitutive modelling. The length to width ratio of mask chips is focused as a main factor in this thesis when preparing MSM samples mixed with Fijian sand. A series of drained triaxial tests is conducted to examine the influence of mask chips on mechanical behavior and properties of MSM. Then, a series of drained biaxial tests is also conducted to examine the influence of shear mode on mechanical behavior and properties of MSM. Next, the critical state theory and a non-associated flow rule are adopted to model the behavior of MSM within the framework of elastoplasticity. A new parameter (p_R) is introduced into the yield function, plastic potential, critical state line and elastic modulus of SIMSAND model to characterize the tensile strength induced by mask chips. As a result, the strength and deformation characteristics of MSM with different relative densities under various loading conditions are properly modelled. All results demonstrate that the proposed model is applicable to construction projects relating to MSM.

PUBLICATIONS ARISING FROM THE THESIS

***Journal papers*:**

[1] Xu WQ, Yin Z-Y, He SH, Yang N. Experimental investigation of mechanical behavior of disposable face-mask chips reinforced-sand under biaxial shear condition. Int. J. Geomech. ASCE, 2024, 24(7): 04024115.

ACKNOWLEDGEMENTS

I would like to express my deepest and sincere gratitude to my admirable supervisor Prof. Zhen-Yu Yin for his selfless dedication and firm support to my Ph.D. work. His profound insight and rigorous research attitude, highly efficient working habit, solid and extensive accumulated professional knowledge deeply expressed me and benefited me a lot. Although I am still far away from being an excellent scientific researcher, he will be my role model to nourish my future work and life. My sincere gratitude goes to Dr Andy Y. F. LEUNG for his selfless help with my research work. I would like to thank all members from Prof. Yin's group; they enriched me with friendship and joy. Special appreciate goes to my lovely friends Dr. Rui Yan, Dr. Qi Zhao, Dr. Xiao-You Wang, Dr. Wei Tian, Dr. Yu-Zhou Wang, Dr. Ying-Lei Li, Dr. Ting-Ting Han for their cordial accompany and support, may our friendship be everlasting. Besides, I would like to express my gratitude to Fei-Long Li for his selfless help and support. Finally, and most importantly, I would like to thank my parents for their understanding, support, and unconditional love.

TABLE OF CONTENTS

LIST OF FIGURES

LIST OF TABLES

Chapter 1 Introduction

1.1 Background

In geotechnical engineering projects cohesionless material has many applications, such as the homogeneous cushion of shallow foundation, filling materials for sub ground equipment or roadbed construction due to its advantages such as high compressibility, excellent drainage ability, low cost, and environmental friendliness of the cohesionless geotechnical material. The most common cohesionless material used in geotechnical engineering is sand. Sand can provide sufficient bearing capacity to the topside structures and drainage tunnels which allow pore water drainage. The usage of sand enhances the stability and drainage capacity of the topside structures. Nevertheless, in real geotechnical project sometimes during the use of the topside structures sand served as the filling material often suffers through excessive external static loading or continuous cyclic loading from the topside structure, which results in sand particle loosing, unevenly distribution, or shearing failure and then leads to instability and even the destruction of the topside structure, or the road surface settlement and collapse. Therefore, many researchers have investigated the influence of additives such as plastic fiber, cement, fly ash, lime, rubber, etc. on the performance of discrete granular materials. The results show that the additives could effectively enhance the shearing strength and improve the deformation, and even increase the adhesion between particles through changing the microstructure of discrete granular particles. However, neither the above-mentioned additives are high cost and environmentally unfriendly nor the improvement effect on the mechanical behavior is not obvious. Recently with the outbreak of COVID-19 pandemic numerous disposable masks have been discarded without proper disposal, leading to serious environmental pollutions. Considering excellent performances of mask such as the flexibility and high tensile strength, the mask chips are regarded as a new additive for the improvement of discrete granular material, which is not only environmentally friendly but also efficient in non-cohesive material reinforcement. There are various factors that will influence the performance of mask chip including the content of mask chips, the shape of mask chips, the surface area of mask chips, the aspect ratio of mask chips, the orientation of masks chips, previous researchers have studied the best content of mask chips for the strength enhancement and the effect of initial mean effective stress on the strength improvement under static and dynamic loading. Based on the best content and mean effective stress the effect of surface area and aspect ratio under different stress conditions have been investigated.

The isotropic triaxial load condition has been selected for experiment simulation to simulate the static load conditions in real geotechnical engineering project. Besides studying the shear band formation which facilitates the explanation of the mechanism of shear failure process the biaxial tests have been conducted. In order to obtain the critical state line and study the effects of confining pressures three different confining pressures have been applied in isotropic triaxial and biaxial shearing tests. Besides, relative density of original granular material will influence the enhancement performance of shear strength of mask chips, therefore two different relative density has been chosen for the isotropic triaxial tests and biaxial tests. Based on the pre-tests and main tests the basic physical properties and geotechnical mechanical properties of pure granular material and the mixture of sand and mask chips can be obtained and the enhancement performance of mask chips can be analyzed. To use the mask chips in real engineering reinforcement project a theoretical model is proposed, while shearing behaviors of discrete granular material is closely related to its current condition, but there is no suitable constitutive model for the prediction of the stress-strain relationships, deformation, the critical state etc. of MSM. Therefore, a state dependent constitutive model based on the critical state theory and non-associated flow rule is proposed under the elastoplastic framework.

1.2 Research Objectives

The main purposes of this research are:

(i)To investigate the effect of the aspect ratio and surface area on the enhancement performance of mask chips under static isotropic triaxial load, with emphasis on the micro-scope observation on particle-to-particle and particle-to-flexible chips interaction during the loading period for the further explanation of the enhancement performance of mask chips, and comparing the geotechnical properties of pure granular material and MSM to observe the enhancement performance of mask chips from macroscope perspective. Moreover, the effect of confining pressure and relative density on the mask chips enhancement performance have been investigated as well.

(ii) To investigate reinforcement performance of mask chips under biaxial load with emphasis on the variation of peak point, stress ratio and volumetric strain. And to investigate the relationship between the parameter denoting the chip size characteristics and enhancement performance.

(iii)To investigate the critical state plane under biaxial loading condition from the inclination, shape and thickness of the shear band and select a best-performing theoretical model for the prediction of the inclination angle of shear band.

(iiii) To propose a new constitutive model tailored to describe the state-dependent mechanical properties of sand and mask chip mixture.

1.3 Research Methodology

The methodologies to reach the objectives mentioned above are (1) laboratory tests including drained triaxial tests and biaxial tests, and (2) constitutive modelling.

1.4 Thesis Outline

This thesis has six chapters, except this chapter introduction, the other five chapters are summarized as follows:

Chapter 2 reviews the conventional reinforcement methods of soil with emphasis on the strengthening effect of mask chips in different geotechnical material. The omissive characteristics of the mask chips and missing factors related to the stress condition have been pointed out. The disabilities of the conventional constitutive model on the description of mask chips-reinforced granular material also have been clarified.

Chapter 3 investigates the basic physical properties and mechanical parameters of the pure discrete granular and mask chip reinforced granular material through conducting pretest experiments and monotonic isotropic triaxial tests. The effect of aspect ratio and surface area of mask chips, the initial mean effective stress, and the relative density of specimen on the shear strength enhancement of discrete granular material under static isotropic triaxial load has been studied.

Chapter 4 studies the mechanical behavior of sand and mask chips mixture under biaxial loading and investigates the optimal size of the mask chips corresponding to the most obvious strength enhancement. The shape, inclination, thickness, and the microscopic development of the shear band have been investigated for the prediction of failure surface. Theories predicting the inclination of the shear band have been compare and selected. A parameter η controlling the relationship between the size of the mask chips and the averaged diameter of sand is proposed to correlate with shear strength enhancement to guide the application of MSM in engineering practice.

Chapter 5 proposes a state-dependent constitutive model for the prediction of the performance of sand and mask chips mixture. The non-associated flow rule, the theory of elastoplastic, and experiment data are used to modify the conventional SIMSAND model by introducing a parameter into constitutive model to direct consider the tensile strength induced by the mask chips. The parameters of the new proposed constitutive model are obtained and calibrated by conventional experiments and curve fitting of the experiment data. The model is validated by comparing the prediction result from the constitutive model with the isotropic triaxial tests data.

Chapter 6 summarizes the main conclusions of present work and future plan.

Chapter 2 Literature Review

2.1 Disposable polypropylene facial mask worldwide

2.1.1 Occurrence of discarded disposable waste

The outbreak and the spread of COVID-19 and increasing demand of personal protective equipment during COVID-19 epidemic

Since the outbreak of COVID-19 and its subsequent spread worldwide, the pandemic that began in December 2019 has resulted in loss of millions of live (Ciotti, Ciccozzi et al. 2020, Haleem, Javaid et al. 2020). Disposable single use facial masks have become an important tool in preventing the spread of respiratory infections in public spaces, as they have been proven the significant ability of reduction the transmission of respiratory droplets and of minimizing the risk of airborne infection. Many counties, such as Germany, Australia and Israel, have enforced the wearing of facial mask in public space prior to 2023 (Betsch, Korn et al. 2020, Li, Liu et al. 2020, Tirupathi, Bharathidasan et al. 2020, Pourebrahimi 2022).

Researchers have found that low-cost facial masks, which have limited effectiveness, are only suitable for a few hours of use during the COVID-19 outbreak. There has been an unprecedented increase in demand and production of masks worldwide. To meet the growing demand, the global production of single use low-cost facial masks has increased sharply. The global use of mask reached a staggering $129 billion per month in the early stage of the COVID-19 pandemic (Li, Liu et al. 2020, Scheid, Lupien et al. 2020, Shetty, Wollenberg et al. 2020, Benson, Bassey et al. 2021, Mejjad, Cherif et al. 2021).

The continuous spread of COVID-19 led to a large-scale consumption and disposal of single used facial masks worldwide. During the peak of the pandemic, the amount of medical waste, including disposable facial mask, reached 240 tons per day only in Wuhan, China. Similarly, significant amount of medical waste has been observed in Thailand, Philippines, Malaysia, India, and other locations (Sangkham 2020).

In addition, researchers have found that due to economic and management reasons, the ability of handling the waste masks in low-income developing counties is insufficient. These discarded masks will inevitably pose a huge threat to the nature environment of low-income developing countries (Chowdhury, Chowdhury et al. 2022). Africa has been the main source of wasted masks in the world. Fifteen out of fifty-five Africa countries are the main waste masks emitters of wasted masks. In Kuala beach, Kenya, a discarded waste masks maybe found every ten square meters (Okuku et al. 2021). A large amount of discarded disposable masks was also found in Turkey with an average of 182 marks per square meter.

Improper disposal of waste masks in the form of household garbage and community garbage

Expecting masks in medical waste, the vast majority of mask that maybe contaminated by COVID-19 are in the form of household garbage or community garbage, and many people casually discarded the mixture of masks and domestic waste. These mixtures are treated as uncontaminated urban waste. The improper disposal of the single used disposable masks has become common in environments such as cities, forests, rivers, beaches, and oceans (Sangkham 2020, Mejjad, Cherif et al. 2021, Tan, Wang et al. 2021).

2.1.2 Hazards of waste masks

Impact of discarded disposable waste masks on the marine environment

Masks are made from a variety of materials and are typically composed of three main parts: the outer layer made of polypropylene and polyester that provides the physical isolation and waterproofing to prevent the water entering and existing the mask; a filter layer made of polypropylene, cellulose or activated carbon that filters the particles, bacteria and virus from air to prevent the wearers from respiratory infection; the inner layer made of soft fibers like cotton or cellulose that provide comfort an absorb sweat (Shruti, Pérez-Guevara et al. 2020, Mobarak, Hossain et al. 2022). Disposable discarded masks pose potential hazards to marine ecosystems and have unpredictable serious impact on marine life. These masks can take hundreds of years to break down thus causing significant harm to marine life. For instance, disposable masks ingested or entangled by animals can cause suffocate and injury (Dharmara et al.2021; Aditya et al.2022; Kumar and Mohapatra, 2022; Wang et al., 2021). In addition to the harm to marine ecosystems and organisms, the adsorption of organic and inorganic nutrients by discarded masks will provide a stable environment for viruses and bacteria, enabling future reproduction of virus and bacteria (). After microbial degradation, photochemical weathering, hydraulic action, and soil erosion in the environment, discarded disposable masks can be gradually damaged, fragmented, and decomposed, thus releasing microplastics. One disposable mask release about 1.5 million microplastics particles. The microplastic source of mask is mostly fibrous, with greater toxicity and adsorption capacity, which is different from the common granular microplastics. It is worth noting that because microplastics are difficult to degrade in the environment, microplastic release from discarded masks are easy to accumulate in the biosphere. Microplastics is a mixture of heterogeneous plastic particles, which is often difficult to distinguish with the naked eye. It is vividly called “PM2.5 in the sea”. Researchers found that because of the small size of the microplastics, it is easy to be ingested into the organism. Entering the food transmission chain through crops and animals poses a threat to human health. The intake of microplastics may be through diet, skin contact and air inhalation.

Disposable masks flowed into the marine environment through a variety of ways such as: rivers, winds, drainage systems, human activities, and shipping routes, most of the mask waste will be transported to ocean currents around the world, while another part of the mask waste will remain at sea surface (Aragaw 2020, Akarsu, Madenli et al. 2021, Dharmaraj, Ashokkumar et al. 2021). Researchers investigated nine coastal areas on Bushehr coast of

Iran and found that the density of the waste mask is the highest on the most densely populated coast (Akhbarizadeh, Dobaradaran et al. 2021). Besides, the disposable masks have been randomly abandoned on the beaches of some unpopulated island in Hong Kong, China, such as Soko beach, Tai O (Bondaroff, Cooke et al. 2020, Luhar, Luhar et al. 2022, Tesfaldet and Ndeh 2022, Rajkhowa and Sarma 2023). Trough personal protective equipment (PPE) monitoring experiment conducted on the world longest beach, Cox's Bazar beach, approximately 29254 pieces of protective equipment were discovered on the beach, of which 97.9% were discarded disposable mask (Rakib, De-la-Torre et al. 2021).

Harm of waste masks to the wild environment

At the same time, a large amount of disposable masks is casually discarded in the wild environment or transported into wild environment through nature means such as wind and river, causing the adverse effect on the physiology of the wildlife. Wang et al. (2022) discovered that the birds in Netherland used the discarded disposable as nesting material, which imply the threat of the discarded disposable mask to the wild environment.

2.1.3 Conventional disposal and reutilization method of waste masks

The disposal of discarded waste masks requires strict operations, such as isolation, sorting, storage, collection, transportation, and final disposal. Some volunteers voluntarily dispose discarded masks in the beach. But due to the lockdown caused by the epidemic, this behavior is difficult to continue (Kaewchutima et al. 2023). Traditional medical waste must be safely disposed of through incineration. But burning medical waste can emit harmful air pollutants (Jayasinghe et al. 2022; Shammi et al. 2021). In addition to incineration, discarded waste masks are also disposed of through landfill. But landfill is a major disaster. In addition to wasting recyclable capital, the wasted masks from landfills pollute soil and water, occupying a large area of land (Sangkham et al. 2020; Sharma et al. 2020). In addition to incineration and landfill, other technologies based on thermochemistry, solvent, and physics are also widely used for the treatment and resource utilization of discarded masks. The process of catalysis pyrolysis can generate a large amount of hydrogen gas, which is an environmentally friendly resource, which can alleviate energy crises. Solvent based technology, as a more convenient and effective method, directly immerses masks in specific chemical reagents to change the original structure of polypropylene and obtain multifunctional materials. Like a battery partition. Other physical technology, masks are mixed with traditional construction material. Physical technology aims to enhance the strength and functionality of traditional materials through modifying the original materials by mixing mask fibers. For example, concrete is a widely used material in construction materials, but it has disadvantages such as low tensile strength, low ductility, and concrete shrinkage. By adding mask fragments mask fibers control the cracking caused by the plastic shrinkage of concrete and increase the resistance of fragmentation of concrete. However, a higher percentage of fibers may reduce the strength of the concrete, as it is difficult to evenly distribute fibers in this quantity. In addition, the stiffness of mask fibers dilutes original material stiffness, resulting in a decrease in the stiffness of the mixture. Polypropylene fiber increases the tensile and elastic strength of the mixture. However, compression strength may be affected, and short fiber may increase the compressive strength because compression failure is also cracking, and fiber can resist cracking, increasing the compression performance of the mixture. Long fiber may be prone to cracking due to their bridging effect, resulting in compressive failure surfaces. At the same time higher density of fiber may dilute the stiffness of the mixture, thereby reducing the compression strength. The barrier effect of polypropylene reduces the invasion of the harmful ions in concrete and has better chlorine resistance, improved the durability and size stability of original material. Novel physical technologies are more environmentally friendly and can produce new properties such as tension, compression, and microbial resistance. In addition, the raw fibers used in the concrete to enhance its performance is expensive. The production of raw fibers, namely carbon fibers consume enormous energy and is believed to increase the emissions of carbon and environmentally harmful ions. Recycled waste masks in the form of fiber provide cheaper resources of fiber as construction materials and may replace existing raw fibers. Therefore, the use of these materials in concrete partially solved the problems of environmental pollution and ecological damage (Ilyas, Srivastava, and Kim 2020; Idrees et al. 2022; Selvaranjan et al. 2021; Ahmed and Lim 2022; Avudaiappan et al. 2023). The effect of content of mask fragments on the mechanical properties of a mixture of mask and Fujian sand under static and dynamic load conditions has been studied. The research results found that the shear strength of Fujian sand added with mask fibers increased and the dilatancy deformation caused by the shear was suppressed, at the same time, the energy absorption generated by dynamic loading was increased (Zhang, Wang and Yin 2022). Some researchers have studied the effect of the content of mask fragments on the mechanical properties of completely decomposed granite and found that the optimal mask fragment content is 5%. In other words, when the content of mask fragments reaches the optimum the increase of the shearing strength reaches the maximum value, if the content of mask fragments continues to increase, the shear strength of the sample decreased accordingly (Xu, Yin and Wang 2022). Some researchers use mask fragments and pulp as additives in concrete (Idrees et al. 2022; Avudaiappan et al. 2023; Parija and Leung 2020). Rehman et al. use waste fiber fragments in fatty clay to improve its mechanical performance. Researchers also explored the role of fibers from crushed waste masks in road and base layer of pavement (Ghadr et al. 2022; Said and Rahhal 2022; Zhang, Wang and Yin et al. 2022). However, there is little research on the effect of aspect ratio and area of mask fragments on the mechanical performance of Fujian sand. This chapter will study the optimal aspect ratio and the optimal area of mask chips from a macro perspective, to maximize the mechanical performance of mixture of mask fragments and Fujian sand.

2.2 Monotonic triaxial test apparatus

Geotechnical monotonic triaxial apparatus is an important testing equipment in the field of geotechnical engineering. Engineers can simulate the stress state and deformation behavior of the underground soil and rock surrounded by isotropic confining pressure under static shearing load by conducting monotonic triaxial tests on rock and soil, thereby helping them evaluate the stability, bearing capability and engineering properties of underground soil and rock.

The triaxial testing apparatus used in this research is manufactured by VJ Tech. The triaxial testing instrument consists of triaxial chamber, axial loading system, confining pressure loading system, digital data acquisition system.

The triaxial chamber achieves confining pressure loading and axial load loading on the specimen. The triaxial chamber is installed between the bottom pressure machine seat and the top crossbeam. The triaxial chamber, also named pressure chamber, is an organic glass cylinder, divided into two parts: a base and an upper cover. The base is equipped with a high intake value clay plate and two drainage pipes. The top plate of the top cover is equipped with a displacement sensor, exhaust plugs and a load transmission piston rod. The base and the top cover relate to T-shaped bolt and sealed with rubber Oring.

The axial loading system is formed of press machine, gear box and load cell. Pressure machine is constitutive of box body, loading frame. There is a pair of worm gear pairs and high-precision ball screws inside of the box body. The gearbox is a gear reduction mechanism driven by a permanent magnet low-speed synchronous motor, and the shaft speed is adjusted by pulling the shaft. There are total of 15 gears with a speed in the range of 0.002mm/min to 4 mm/min and the shaft lifting speed is adjusted according to the experiments personal need. There is a shaft lifting meters on the cabinet for experimental personal check.

A load cell is installed on the cross beam of the loading frame to accurately apply the vertical load. There is an LVDT fixed on the center axis of the load cell to monitor the deformation of the stress ring through making the tip of the LVDT iron core exactly touch the center of the bottom of the stress ring. The displacement of the stress ring monitored by LVDT is then converted into electronic signal data, which is an equivalent value to the shearing load applied through axial loading system on the top of the specimen.

The confining pressure loading system consists of pressure panel and air water cylinders aiming to accurately applying the confining pressure on the soil specimen. The pressure panel enables the water and compressed air to correctly be distributed to the right equipment to undertake a triaxial test through controlling the cell pressure and back pressure. A press gauge is included so that known pressure can be applied on the specimen using the pressure regulators fitted to the panel. Air water cylinders provide an interface between water and compressed air during the confining pressure applying process. They contain a rubber bladder which is filled with compressed air to pressurize or decompress the cell pressure and back pressure for the triaxial test. The pressure applied by the confining pressure system is limited by the air compressor controlled by the HMO department.

Three water pressure transducers monitoring the isotropic confining pressure, back pressure and pore water pressure are connected to the water drainage pipes.

The automatic volume change device is developed to precisely measure the volume change of pore water distributed in saturated specimen during the test. An external data logger is used to capture and transmit the LVDT readings and automatic volume change device readings taking during the test to the outside computer system. The changing volume within the cylinder moves the piston, which is connected to a small range LVDT to record the measured data. The top chamber has a volume capacity of 100ml. When used in conjunction with the bottom changeover device the volume capacity of the top chamber becomes infinite. The bottom changeover valve box is working in conjunction with the drainpipe.

The data from the transducers during the test can be visualized and stored by an automatic computer system such as VJ Tech's Clisp Studio. A computer and a software package is needed for the automatic computer system installation.

The triaxial apparatus has multiple functions such as consolidation test, shear strength test, compression test, which provide methods to measure and analyze soil physical parameters and soil mechanical properties. Although the testing time of static triaxial test is long and the cost of test equipment is high, the geotechnical triaxial apparatus applies precise stress to soil samples and control different stress path and surrounding confining pressure through the load loading system and confining pressure loading system to simulate the real stress state of soil specimen in various engineering scenarios. Based on the triaxial apparatus a series of monotonic triaxial tests of soil and rock can be conducted, providing some basic soil parameters and stress-strain relationships of soil specimen under static loading. In summary, monotonic triaxial test is an effective method for studying the mechanical behavior of assorted soil material.

2.3 Constitutive model for description of mechanical behavior of fiber reinforced material

To predict the mechanical properties of the fiber reinforced material, the fiber reinforced soil was defined as a composite comprising of fiber phase and base phase, therefore, elastic linear model and Mohr-Coulomb model tailored for fiber phase and base phase respectively are superimposed for the establishment of a two-phase constitutive model to predict the mechanical properties of fiber reinforced soil. Wang et al. (2014) developed a nonlinear constitutive model based on Diambra's model which is composed of modified Cambridge model and liner elastic model to predict the nonlinearity behavior of the fiber and set failure criterion for fiber reinforced soil at large strain condition through introducing Gao's strength theory. Model validation results show that Wang's model could well predict the nonlinearity of the stress-strain relationship of the fiber reinforced soil and analyze the yield condition of the reinforced soil. Villard et al (1990)'s model used to consider the effect of fiber distribution orientation on fiber reinforcement through introducing a variable reflecting fiber orientation influence in the model. Geetha et al. (2014) proposed an anisotropic constitutive model based on modified Cam clay model for fiber reinforced soil. To further capture the anisotropic behavior of fiber reinforced soil under multiaxial stress condition a new model has been proposed by Gao et al. (2021) through considering an anisotropic parameter denoting relative orientation between the loading direction tensor and fiber orientation tensor. Persid and Craig (2023)'s model is developed to simulate the degradation of the cohesive bond at the fiber-soil interface and the elastoplastic behavior of the fiber. In fiber reinforced soil fibers form a network which may absorb energy from external load and disperse the stress when soil suffers through external compression load so that the tension strength and ductility of reinforced soil is enhanced. Friction and bonding between fiber and particles disperse stresses to a larger scale so that the stress concentration between particles is reduced and the overall strength and stability of the fiber reinforced soil is improved. Mask chips in reinforced soil could occupy the void between particles, increasing the degree of density and the overall stability. Besides, the surface characteristic of mask chips prompts internal interlocking of soil particles to form a more stable soil structure, increasing the cohesion and shear strength. There is a great difference in the microscope behavior of fiber reinforced soil and mask chips reinforced soil, therefore, the constitutive model tailored for fiber reinforced soil is not able to well describe the behavior of mask chips reinforced soil. In our work a new constitutive model for the mask chips reinforced soil is proposed.

Chapter 3 Investigation of Strength and Deformation Properties of Enhanced Granular Material under Static Load and Three-Dimensional Confining Pressure

3.1 Introduction

This chapter aims to investigate the influence of the aspect ratio and area of geotextile chips on the mechanical behavior of granular material under one dimensional static loading surrounded with isotropic confining pressure. A series of undrained monotonic triaxial tests were conducted to obtain the stress strain relationships and volumetric change of pure granular materials and mixture of original granular material and geotextiles fragments of different aspect ratio and area. Before the conduction of a series triaxial tests several basic geotechnical tests were conducted. The influence of the mask chips in various shapes on the elementary physical properties of pure granular materials (initial void ratio, specific gravity, particle size distribution curve) was investigated. The test material, apparatus, and test program and test implementation are presented in the following content. The test results indicate that a moderate increase of the aspect ratio and area of the mask chips can increase the shear strength of the discrete granular material. The mask chips added in the discrete granular material can suppresses the dilatancy deformations of the medium dense granular material, however, for higher dense discrete granular material the inhibition effect on the dilatancy deformation of original granular material caused by the additive geotextile chips is not obvious. The additive geotextile fragments increase the elasticity of granular materials and lower the stiffness of the granular material at half compression strength. In addition, the study on the influences of relative density and effective confining pressure on the improvement of shearing behavior of discrete granular material is supplementary and can guide the usage of geotextile fragment in granular material at great length.

3.2 Test material and scheme

3.2.1 Test material

Basic properties of granular material

Test material used in this work is Fu Jian sand since the abundant production of Fu Jian sand increases the repeatability of the experiment for the results comparison and verification and its wide engineering application, providing the strength and stability of the concrete and a stable support and drainage function of the roadbed.

To investigate the particle size effect, particles with a diameter larger than 1.18mm and lower than 0.6mm were avoided after sieving. Table 3.1 shows the basic physical characteristics of scaled-down sand. A definitive method small pycnometer method is used to determine specific density G_s of soil particles with particle size finer than 2mm, according to Geospec3-Clause 7.2 (2001). The maximum dry density is determined by compaction tests repeated three times using a 4.5 kg rammer (Geosepc3-Clause 3.7) and the minimum dry density is determined by the large volumetric bottle method. The maximum void ratio and minimum void ratio can be calculated based on maximum dry density and minimum dry density using the following equations:

$$e_{\min} = \frac{\rho_w \times G_s}{\rho_{\mathrm{dmax}}} - 1 \qquad (3\text{-}1)$$

$$e_{\max} = \frac{\rho_w \times G_s}{\rho_{d\min}} - 1 \qquad (3\text{-}2)$$

where ρ_w is the water density at room temperature, G_s is the specific gravity of scaled-down sand particles, $\rho_{d\max}$ and $\rho_{d\min}$ are the maximum and minimum dry density of scaled-down sand particles respectively. Fig. 3.1 displays the particle distribution curves of the original granular sand and scaled-down sand.

3.2.2 Test apparatus

The monotonic triaxial test with controlled confining pressure and vertical load was conducted on a triaxial testing loading frame and unit. The triaxial cell for measuring the shearing behavior of the test specimen under static loading is placed on the lifting table of the load unit. The test data acquired during the whole process of the test is logged by the associated data logging system. The room temperature is maintained at 25 degrees Celsius by central air-conditioning to make sure all the test is carried out at room temperature. The main components of the test apparatus providing a support to a smoothly conduction of a triaxial shearing tests have been introduced in detail.

The loading frame of the triaxial test is specially designed for monotonic triaxial test. The maximum load capability of this loading frame is 250 KN and has proven reliability. This load frame is an old version without a built-in channel data logger and USB or internet connection to PC. An incremental vertical load is enabled to be applied to the top cap on the test specimen through a load cell and this loading frame. The compression data logging during the loading period is completed by a data acquisition system consisting of a small LVDT measuring physical quantity in the form of an electrical signal, a data logger digitizing the electrical signal and transmitting a binary data and a computer with specialized software installed to check and store the data. The detailed introduction of small LVDT and data logger is shown. Three out-built water pressure transducers were installed on the drainage pipes (cell water pressure drainage pipe, back water pressure drainage pipe, pore water pressure drainage pipe, respectively) and connected to the outside display screen through 8mm high-density polyurethanes drainage cables. Similarly, detailed information introducing the water pressure transducer and display screen of water pressure are shown. It is noteworthy that the largest particle size of the test material is 1.18mm, which is hundredth of the diameter of the test specimen that eliminates the edge confining effect on the shearing behavior of discrete granular materials under compression loading condition. The thickness of the rubber membrane is only 0.05mm and the external diameter of the rubber membrane is equal to that of the test specimen, which attenuates the confining force around the test specimen induced by the rubber membrane. The triaxial cell is capable of withstanding 5000kPa confining pressure.

3.2.3 Test apparatus calibration

Two calibrations are implemented before the real test. The first one is to calibrate the shrinkage factor of automatic volume controller, which is of importance to capture the real volume change of the specimen during the test period. For calibration the automatic volume controller is directly connected to the water tank. For the convenience of the illustration, an acronym AVC is adopted on behalf of the automatic volume controller. The second one is the calibration of the load cell. This is crucial for the calculation of the deviatoric stress in the behavior analysis during the shearing process. It is noteworthy that to facilitate the calibration implementation the triaxial chamber and the test sample in it were replaced by rigid bricks, and a reference load cell (digital Load Calibrator 0-10KN, VJ Tech) is used to quantize the real compression force.

The volume change controller is calibrated by defining the relationship of the real volume of the water passing through the automatic volume controller drained from the top water tank and the reading of the small LVDT fixed vertically on the AVC. To avoid mechanical errors and personal measurement error the process of calibration of the AVC is repeated three time, and in each calibration, totally three points marked on the piston road are measured. Fig. 3.2 shows the shrinkage equation of the initial data measured for the calibration of AVC. The solid black line is the finalized calibration line of AVC. The slope of the solid black line is the shrinkage factor for the initial data captured by AVC. The other two dash curves stand for the real relationships between the actual volumes of the water passing through the AVC and the initial reading captured by the AVC while the piston moves upward and downward respectively. Two nearby dashing straight line crossing through the end of the dash curve represent the formulized fitting lines for the ease of modifying the calibration in correlative software.

The load cell is calibrated by finding the relationship between the initial reading captured by LVDT fixed on the load cell and the actual load measured by a reference load cell. It is noteworthy that the reading of LVDT is stored and accessible from the computer software *Clisp* developed by VJ Tech. The calibration line of load cell is shown in the Fig. 3.3 as a solid straight line and the associate calibration equation is expressed as a first order equation in the Fig. 3.3. The calibration equation can be used to modify the initial reading collected by LVDT to output the real compression force.

3.2.4 Test specimen preparation

Sieving is done before the preparation of the test material to retain the test particles within the range of particle size between 0.6mm to 0.85mm and 0.85mm to 1.18mm and the particles from above mentioned two size groups were mixed in a ratio of 7:3 which is determined according to the particle size distribution curve as shown in Figure 3-1. The nature dry densities ρ_d of the mixed granular material with two kind of different relative densities was determined by the following equation:

$$\frac{\rho_\omega \times G_s}{e+1} = \rho_d \qquad (3\text{-}3)$$

Where ρ_ω is the density of water at room temperature, $G_s$is the specific density of granular materials, and e is the void ratio of granular material. All the value of the parameters contained in the left equation are displayed in the Table 3.1. Then the masses of the granular material are obtained by multiplying the calculated nature dry densities ρ_d and a constant test specimen volume. To make sure the uniformity of the specimen during the packing processes the prepared granular materials were evenly divided into five groups and put in five beakers. Reinforcement geotechnical fabric material which is discarded mask were cut into three different shapes and were divided into five parts as well to uniformly prepare the specimen.

According to what decided the content of mask chips and the mask chips were weighted and to make a uniformly distributed sample the mask chips are also divided into five parts.

Cut the geotextile into three different shapes, and the total weight of the geotextile chips is 5% of the total weight of the granular material, and the geotextile mixture is also divided into five groups.

3.2.5 Test scheme and test implementation

Totally twenty-four monotonic triaxial tests were conducted on granular material reinforced by disposable mask chips with two kind of different cross areas and two kinds of different aspect ratios to investigate the influence of cross section area ($36mm^2$, $100mm^2$) and aspect ratio (1:1, 4:1) of disposable mask chips on the enhancement effect of the shearing behavior of discrete granular material. Detailed test scheme is listed at Table 3.2. For the basic raw material, particles with different particle sizes were all uniformly distributed, only the density of the basic raw material would be different, therefore to exclude the impact of the relative density of the basic material and to ensure that only the effect of shape characteristic of mask chips on the shearing behavior are studied in all triaxial tests, all the relative density of the basic material are studied. The first twelve tests investigate the response of high dense basic material to the additive mask chips, the rest twelve tests investigate the response of medium dense basic material to the additive mask chips (In order to compare the effect of the shape characters of mask chips on the shearing behavior of discrete granular material with different relative densities, the first twelve tests performed on the high dense granular material and the rest twelve tests performed on medium dense granular materials). To obtain the internal friction angle representing as the slope of the shearing critical state line and investigate the influence of the confining pressure on the test results three kinds of different effective confining pressure (50kPa, 100kPa, 200kPa) were selected. To keep the pore water pressure of the saturated specimen constant the vertical load was applying on the specimen by lifting the platform at a constant rate of 0.6mm/min.

According to the reference 15% axial strain is enough for the specimen to go through the failure and to ensure the whole procedures of shearing process were recorded for the tests in the monotonic triaxial tests 18% axial strain is achieved. Each monotonic triaxial test consists of six stages which are sample preparation, initial confining pressure application, carbon dioxide injection, specimen saturation, specimen consolidation, constant rate loading. After the completion of the specimen preparation, the water from the top tank was injected into the triaxial chamber and 15kPa initial confining pressure was applied on the specimen to prevent the specimen from collapse and the triaxial membrane from swelling. Then 8kPa carbon dioxide was injected into the test specimen for 8mins to replace the air between specimen particles to facilitate the sample saturation because the carbon dioxide is easy to be dissolved in the water than air. After the completion of carbon dioxide injection continuously increasing the confining pressure and back pressure at the same time in an increment of 30kPa each time to complete the saturation of the sample. For our test when the incrementation of the confining pressure and back pressure reaches 300kPa a B check is conducted to determine the saturation condition if the B value is larger than 95% then the saturation is completed otherwise repeat the above steps until B value is larger than 95%. After the completion of the sample saturation the isotropic sample consolidation is conducted by increasing the confining pressure to the predetermined value. The series of monotonic triaxial tests in this chapter conducted drained consolidation. During the consolidation process, the sample receives the isotropic compression pressure which allowing the pore water between the specimen particles drained through the pipeline. The volume of the discharged pore water was monitored by AVC to facilitate the calculation of the change of the sample height during the consolidation process. When the volume of the pore water doesn’t change then an equilibrium between the compression force and the resistance force provided by skeletal particles and void particles were reached, which means the isotropic compression is completed. After the completion of specimen consolidation, the confining pressure and back pressure was maintained constant, and the compression load is started applying on the specimen through lifting the platform as a rate of 0.6mm/min until the axial train reaches 18% of initial height of the specimen. The data of deviatoric force and the volume change logged during the loading period are stored and accessible in the computer for the following data analysis.

3.3 Results discussion

Monotonic triaxial tests were conducted on pure granular material and mask reinforced sand.

Table 3.3 and 3.4 show the effect of relative density, effective confining pressure, shape characteristics of mask chips on the initial modulus and secant modulus at 50% compressive strength of granular material. It is obvious that the higher the confining pressure the larger the secant Young’s modulus at the middle of the peak deviatoric stress due to the larger confining pressure restrain the particle movements, leading to stiffer sample under higher confining pressure. The same as the confining pressure, the higher the relative density the larger the secant Young’s because skeleton provided by more particles results in larger shear strength before critical state. However, due to the flexibility of mask chips with the inclusion of mask chips the secant Young’s modulus of reinforced sand became smaller. In particular, the confining pressure, mask chip shape characteristics and relative density almost have no influence on the specimen stiffness at small axial strain condition, reflected on that the initial Young’s modulus almost is the same shown in Table 3.3.

Table 3.5 shows the effect of additive different shaped geotextile chips on the dilatancy angle of granular material and mixture with different relative density under different effective confining pressure ($\boldsymbol{\sigma_c'}$). The higher the relative density, the larger the dilatancy angle due to the pronounced particles interlock, particles were getting closer to each other, leading to more obvious dilatation volumetric strain, the effective confining pressure and shape characteristic do not have an obvious influence on the dilatancy angle.

From Table3.6, obviously, the relative density, effective confining pressure and shape characteristic of mask chips do not have influence on the Poisson’s ratio.

Fig. 3.4 shows the performance of pure granular material under a static loading and the strain ratio keeps constant as 0.06mm/min. Deviatoric stress-strain relationships of pure granular material under different confining pressure with medium and high relative density are presented in Fig. 3.4(a).Fig. 3.4(a) shows the relationship between the deviatoric stress and the axial strain of pure sand with relative density of 60% and 90% under three different confining pressure of 50kPa, 100kPa and 200kPa. The pure sand with relative density of 90% has higher peak strength because the dense pure sand goes through a limit state of strain hardening before entering the strain softening stage. The residual stresses of the pure sand with the relative density of 90% and 60% are almost the same, especially for the sand under low confining condition. The reason may be that the frictional forces (composed of internal frictional force and interlocking force) between the failure surfaces are almost the same (due to the similar shape of the failure surfaces and the similar critical void ratios between the sand sample with different relative density). For pure sand surrounded with higher confining pressure the duration of particle movements before the failure is longer which may result in different failure surfaces or critical void ratio. The stiffnesses represented by the initial Young’s modulus of the pure sand with relative density of 60% and 90% under different confining pressures are almost the same because the difference of initial void ratios is not that significant thus the initial stiffness difference under low stress conditions can be ignored.

The influence of the relative density and the confining pressure on the initial stiffness quantified by the initial Young’s modulus can be ignored because the stiffness of dense sand and medium dense $(Dr_{dense\ sand} = 90\%, Dr_{medium\ dense\ sand} = 60\%)$ sand under low internal stress conditions are have little difference, while at relative higher sample internal stress condition the relative density and confining pressure play an important role on the stiffness because more particles provide the supporting force to resist the deformation.

The peak compression resistance of high-density granular material is higher than that of medium density pure granular material because more particles provide skeletal force, locking force and frictional force (both static frictional angle and dynamic frictional angle play a role in compression resistance), while the residual compression resistance of the high-density granular material is almost the same as that of the medium density granular materials because only the dynamic frictional force were left and the dynamic frictional force provide by the particles on the failure surface have little difference for high-density granular material and medium dense granular material.

The relative density has a great influence on the compression and dilatancy processes. The compression behavior for the sand with lower relative density is more obvious and last longer because more pore that allow sand particles fill in exist between loose granular particles, while the dilatancy happens earlier and more obvious for dense sand than that of loose sand since the dense particles are more prone to mismove, roll, lift and pull out, resulting in an increase of the pore volume between soil particles.

Besides, the confining pressure also affects the sample deformation, which means the higher the relative confining pressure the more obvious the compression process and the less obvious the dilatation process. From a microscope point of view to explain this phenomenon is that during the loading period the restriction resulting from medium and minimum confining pressure on the horizontal displacement of the sand particles cause the sample particles to move downwards to fill the voids instead of a particle rolling or a particle lift which generates the void, therefore, intensify the compression process and suppress the dilatancy process.

Two straight lines without makers in Fig. 3.4(b) are the linker of three points in q-p’ space for dense sample and medium dense sample respectively, at three different residual states caused by the confining pressure. for high dense test material and medium dense test material. Critical state lines in $p' - q$ space indicating the failure condition are almost overlapped because the sliding resistance force on the sliding failure are almost the same, especially under the low confining stress condition.

Table 3.1 Basic physical characteristic of scaled-down granular material

Basic characteristics	**Magnitude**
Specific gravity (G_S)	2.637 ($g\ /\ m^3$)
Maximum dry density (ρ_{dmax})	1.664 ($g\ /\ m^3$)
Minimum dry density (ρ_{dmin})	1.398 ($g\ /\ m^3$)
Maximum void ratio (e_{max})	0.882
Minimum void ratio (e_{min})	0.582

Table 3.2 Test scheme of saturated monotonic triaxial tests of pure granular materials and granular materials reinforced with mask chips

Test No.	**Relative density (%)**	**Specimen composition**	**Confining pressure (kPa)**		**Aspect ratio of MSC**	**Area of MSC (mm^2)**
1	60	GM	50		/	/
2			100			
3			200			
4		GM&MSC2005	50		4:1	100
5			100			
6			200			
7		GM&MSC1010	50		1:1	100
8			100			
9			200			
10		GM&MSC1203	50		4:1	36
11			100			
12			200			
13	90	GM	50		/	/
14			100			
15			200			
16		GM&MSC2005	50		4:1	100
17			100			
18			200			
19		GM&MSC1010	50		1:1	100
20			100			
21			200			
22		GM&MSC1203	50		4:1	36
23			100			
24			200			

Table 3.3 The effect of additive different shaped geotextile chips on the initial Young's modulus of granular material and mixtures with different relative density under different effective confining pressure (σ'_c)

Initial elastic modulus (MPa)	Relative density (%)	Effective confining pressure (kPa)	GM	Mixt2005	Mixt1010	Mixt1203
E0	60	50	26.945	7.784	26.946	26.945
		100	26.945	26.845	26.945	26.945
		200	26.945	26.945	26.945	26.945
	90	50	26.976	26.945	27.013	26.946
		100	26.945	26.968	27.08	26.945
		200	26.945	26.945	26.959	26.945

Table 3.4 The effect of additive different shaped geotextile chips on the secant modulus at 50% compressive strength of granular material and mixtures with different relative density under different effective confining pressure (σ'_c)

Secant modulus (MPa)	Relative density (%)	Effective confining pressure (kPa)	GM	Mixt2005	Mixt1010	Mixt1203
E50	60	50	26.794	7.980	20.036	10.560
		100	26.794	31.991	12.889	12.855
		200	35.159	18.337	17.013	18.412
	90	50	10.560	11.818	9.981	10.361
		100	39.645	14.740	12.306	11.670
		200	46.831	23.051	20.682	26.181

Table 3.5 The effect of additive different shaped geotextile chips on the dilatancy angle of granular material and mixtures with different relative density under different effective confining pressure ($\boldsymbol{\sigma_c'}$)

Dilatancy angle (°)	Relative density (%)	Effective confining pressure (kPa)	GM	Mixt2005	Mixt1010	Mixt1203
ψ	60	50	9.509	8.365	12.176	9.501
		100	6.813	9.367	11.473	9.905
		200	6.345	10.694	9.475	9.897
	90	50	14.014	16.608	14.466	9.099
		100	11.205	13.779	13.780	10.498
		200	11.421	11.584	11.923	8.536

Table 3.6 The effect of additive different shaped geotextile chips on the Poisson's ratio of granular material and mixture with different relative density under different effective confining pressure ($\boldsymbol{\sigma_c'}$)

Poisson's ratio	Relative density (%)	Effective confining pressure (kPa)	GM	Mixt2005	Mixt1010	Mixt1203
γ	60	50	0.475	0.350	0.421	0.468
		100	0.442	0.439	0.247	0.453
		200	0.471	0.441	0.431	0.458
	90	50	0.452	0.450	0.428	0.438
		100	0.446	0.440	0.482	0.447
		200	0.463	0.420	0.414	0.446

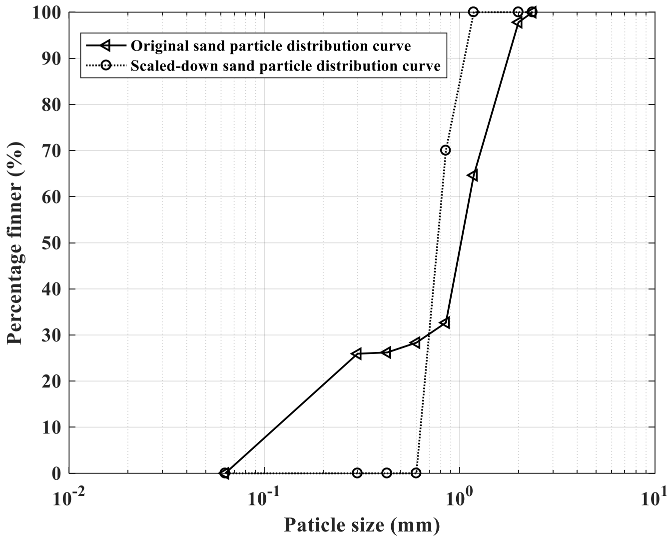

Fig. 3.1 Particle size distribution of original granular material and scaled-down granular material

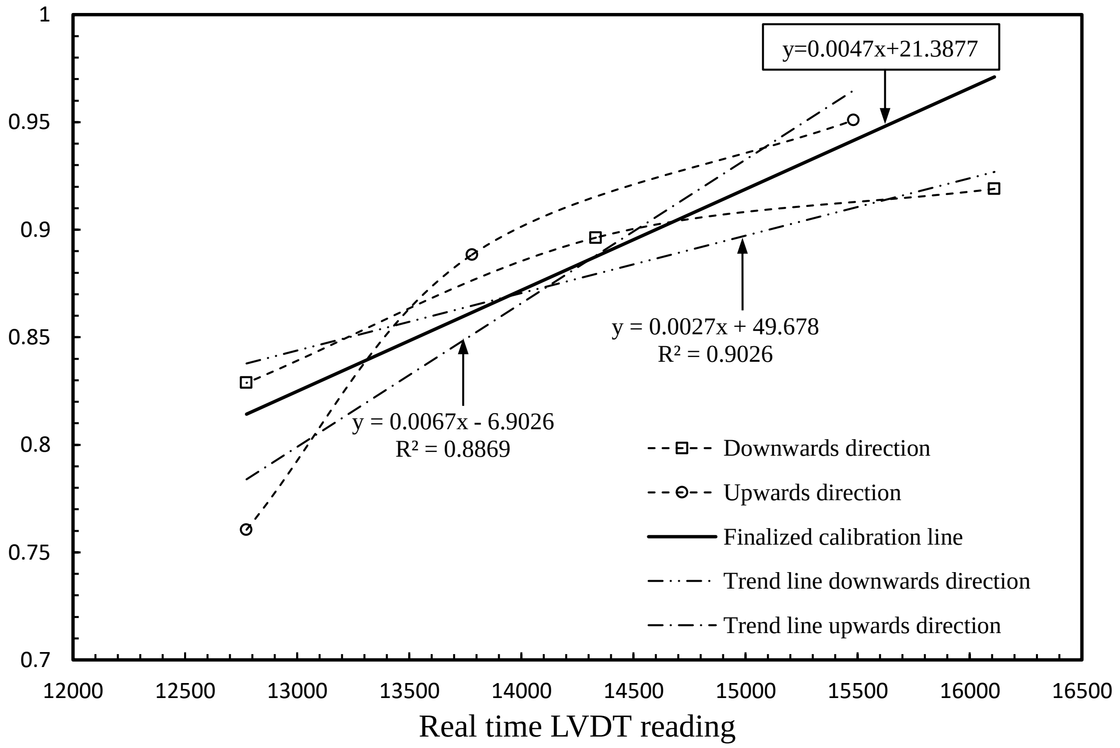

Fig. 3.2 Calibration curve of shrinkage factor of automatic volume controller

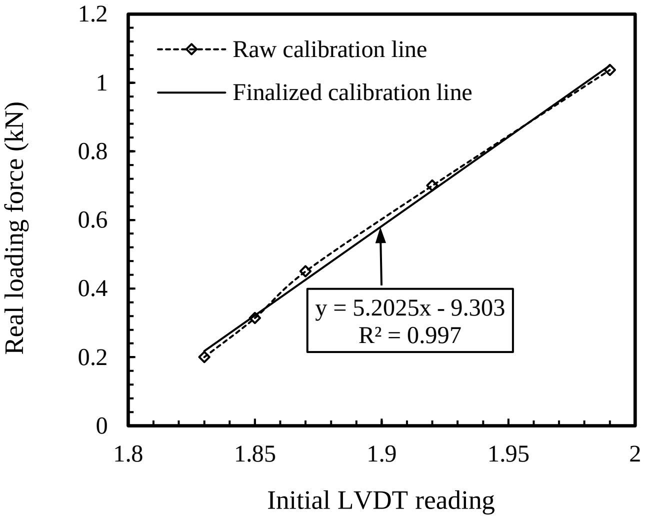

Fig. 3.3 Calibration line of compression force measured by load cell

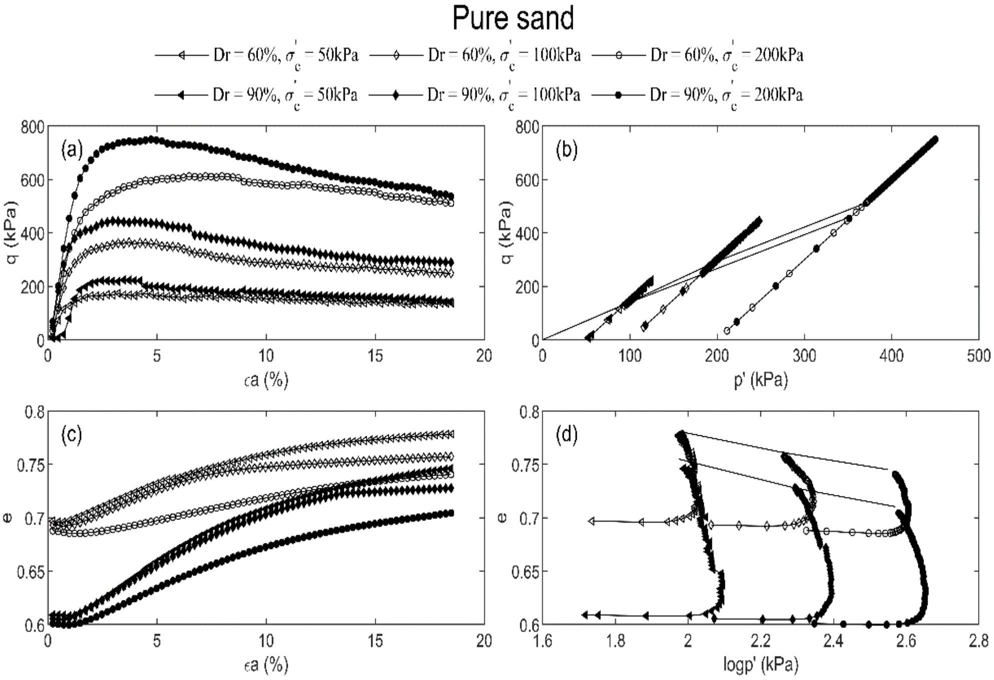

Fig. 3.4 Mechanical properties and critical state lines of pure sand: a) deviatoric stress and axial strain relationships; b) deviatoric stress and mean effective stress relationships & CSL in *p'*-*q* plane; c) void ratio and axial strain relationship; d) void ratio and *Logp* relationships & CSL in *Logp'*-*e* plane

Chapter 4 Experimental Investigation of Mechanical Behavior of Disposable Face-Mask Chips Reinforced-Sand under Biaxial Shear Condition

4.1 Introduction

In recent years, the coronavirus pandemic (COVID-19) has profoundly affected individuals worldwide. Among the most significant and visible preventive measures is the widespread adoption of face masks, primarily composed of polypropylene, to mitigate virus transmission (Lunag et al. 2023). A model developed by Nzediegwu and Chang (2020) estimated that approximately 6.88 billion face masks (about 206,470 metric tons) are produced worldwide each day. The subsequent disposal of these used masks, either through landfilling or incineration, has sparked concerns about their environmental impact (Hossini et al. 2021; Vaverková et al. 2021). Consequently, exploring innovative methods for treating and managing these medical waste products to minimize their ecological footprint is crucial.

In mask management, disinfection is a critical first step aimed at preventing further viral spread. A variety of techniques, spanning from traditional methods such as incineration and pyrolysis, to innovative approaches like dry heat technology, have been developed for this purpose (Asim et al. 2021). Unlike traditional methods, dry heat technology preserves the mask structure, enabling the recycling and reuse of masks or their components, such as polyethylene (Amy et al. 2020). Based on these disinfection methods, recent research has explored the possibility of recycling used masks in civil engineering to valorize them. To be specific, disposable masks, composed of non-biodegradable plastics, can take hundreds of years (around 450 years) to degrade in the natural environment (Karaivanov et al. 2021). Thus, when sterilized using dry heat technology, these masks remain undamaged and can be repurposed as soil reinforcement materials. This not only offers an environmentally friendly waste management solution but also contributes a resource to the construction industry.

In geotechnical engineering, soil reinforcement is considered an effective ground improvement method. This technique has been successfully applied in diverse scenarios, such as slope stabilization, road subgrades, embankments, and reclamation projects (Palmeira and Góngora 2015; Xu and Yin 2016). Soil reinforcement has a long history. In its early stages, natural fibers, including plants, were incorporated into soil to enhance its overall structural integrity and strength (Maheshwari et al. 2012; Wang and Chouw 2017; Wang et al. 2017). Later, polymer materials, such as polyester and polypropylene, are adopted as reinforcement materials due to their high tensile strength, durability and flexibility (Gui et al. 2022; Miranda Pino and Baudet 2015; Priyadarshee et al. 2014; Tang et al. 2022). The fibers mixed within the soil serve as tension-bearing elements, which not only enhances the overall strength properties of the soil but also impacts other soil characteristics. Besides, materials such as glass and carbon fibers (Lv et al. 2021; Sujatha et al. 2021; Wang and Brennan 2019), have also been used to reinforce soil. At present, a variety of geosynthetic materials in various shapes and types, including geotextiles, geogrids, and geocells, are available in soil reinforcement, which could provide significant strength and stability to soil (Hassoun et al. 2018; Mirzaalimohammadi et al. 2021). These materials have significantly expanded the capabilities and applications of soil reinforcement techniques. However, mask chips present a unique case. Their properties, including tensile stiffness, strength, and surface area, differ considerably from those of currently used reinforcement inclusion materials. Consequently, there is a notable gap in comprehensive research exploring their mechanical behavior.

To date, several research initiatives have successfully demonstrated this potential. For example, Sebarian et al. (2021) incorporated shredded face masks into recycled concrete aggregate for road base and subbase applications, resulting in an increase in strength, stiffness, ductility, and flexibility of the blends. Zhang et al. (2022) evaluated the static and dynamic behavior of granular soil reinforced by mask chips, revealing the potential of the mask as reinforcement in granular soil. Xu et al. (2022) conducted monotonic triaxial tests on completely decomposed granite soil reinforced with mask chips, demonstrating that the chips could reinforce clay at the optimum content. Indeed, these findings indicate that employing disposable mask chips as soil reinforcement material is a feasible and sustainable approach. However, further research is essential to comprehensively understand the reinforcement effects under various loading conditions and optimize this innovative solution. Among different conditions, the biaxial shear has been widely adopted because of its ability to simulate complex stress states and generate valuable insights into shear band formation (Han and Drescher 1993; Wang et al. 2022). Yet, this method has not been applied to the study of sand reinforced by mask chips.

This study aims to investigate the mechanical performance of sand reinforced with disposable mask chips under biaxial shear conditions. Mask chips of various sizes (20 mm × 5 mm, 10 mm × 10 mm, and 12 mm × 3 mm) are mixed with Fujian sand at the same content (0.5% by mass), and then a series of monotonic biaxial tests are conducted to investigate the mechanical behavior of the reinforced sand, together with image recording. Tests on pure sand are also conducted for comparisons. The stress-strain behavior and strain-strain relationship are analyzed, and the shear band characteristics are identified and compared.

4.2 Materials and methods

4.2.1 Tested Sand

Fujian sand was adopted in this study as the tested soil. The particle size distribution (PSD) is shown in Fig. **4.1** and the basic parameters are listed in Table 4.1. The tested material is poorly graded granular soil, with the C_u = 1.28 and d_{50} = 0.78 mm. The sand was dried in the oven for 24 h and then prepared as dense samples (D_r = 90%), and the dry density ρ_d

was 1.665 g/cm^3. Moreover, the sphericity and aspect ratio of this material is 0.796 and 0.613, respectively.

4.2.2 Adopted disposable face mask

The clean face mask was utilized in this study for the sake of safety. The adopted mask is the disposable medical face mask produced by Ever Sharp Mask (China) Limited. The top and bottom layers of the mask are made of nonwoven fabric, while the middle layer is the polypropylene melt-blown filter. More details on the mask including physical parameters could be found in (Xu et al. 2022).

The ear loops and metal trips were removed before the masks were cut into chips manually. The rectangular chips were prepared in three sizes, 20 mm × 5 mm, 10 mm × 10 mm, and 12 mm × 3 mm in length and width respectively, to investigate the effect of area and aspect ratio.

4.2.3 Sample preparation and testing plan

There were four groups of samples in total, one group was composed of pure sand and the other three were sand mixed with mask chips, where mask chip sizes were 20 mm × 5 mm, 10 mm × 10 mm, and 12 mm× 3 mm, respectively. Biaxial compression tests were conducted to investigate the reinforcement effect of the mask chips under plane strain conditions. The specimen for the biaxial experiment was in rectangular shape with a length, width, and height of 70 mm × 70 mm × 160 mm respectively prior to consolidation. Consequently, each specimen required 1305.42 g of dried sand (= 1.665 g/cm^3 × 784 cm^3). All specimens had identical initial void ratios. The mask chips were mixed with sand at the mass ratio of 0.5%, i.e., 6.53 g for each specimen except for the pure sand sample. Pre-weighed sand and mask chips were first divided into four sets equally according to their mass (i.e., 326.36 g sand and 1.63 g mask chips per set), then added to four dry containers and mixed with a scoop manually to disperse the mask chips evenly in the sand (Fig. **4.1**). Spraying water on the mixture was also adopted to improve uniformity. These four sets of the mixture corresponded to four layers of the specimen later. To aid the visual observation during the test, the grids of 2 mm × 1 mm were marked on the membrane in advance. After the membrane was fixed on the base with the help of a split mold, the sand-mask mixture was added slowly into the mold, with the porous stone and filter paper in the bottom, and the height of each layer was controlled using a caliper. After a vacuum pressure of around 15 kPa was applied to the sample, the mold was removed, and two glass plates were fixed on opposite sides of the sample to ensure plane strain conditions ($\varepsilon_2 = 0$ as shown in Fig. **4.2**).

The biaxial compression tests were consolidated and drained tests and the axial loading rate was set as 0.6 mm/min. To achieve saturation, the specimen underwent a gradual percolation process with deaired water flowing from bottom to top. In the case of the mask-sand mixture sample, the specimen was left submerged in deaired water for an extended period of approximately 2 hours after flushing. The chamber and back pressure were incrementally increased in synchronized steps, with the specimen drainage valves open. The pressure increments were set at 30 kPa per step, allowing ample time between increments for the pore-water pressure to equalize across the specimen. Throughout the test, the pore pressure parameter B was monitored continuously, which is defined as

$$B = \frac{\Delta u}{\Delta \sigma_3} \qquad (4-1)$$

where Δu represents the change in pore pressure resulting from a change in chamber pressure ($\Delta\sigma_3$) when the specimen drainage valves are closed. When the B value exceeded 95%, specimens were saturated. During our testing, the B value for all samples consistently surpassed 95% when the back pressure reached approximately 250 kPa. For each group, different effective lateral pressures, including 50 and 100 kPa, were adopted in the tests. The tests ended when the axial strain of the specimen reached 18%, where the principal stress was considered stable.

4.3 Results

4.3.1 Stress-strain relationship

Fig. **4.3** presents the variation of the principal stress ratio concerning the major principal strain, which exhibits an initial increase up to a peak, followed by a subsequent decline. Notably, the addition of mask chips results in a significant enhancement in the sample strength under the same lateral pressure conditions. Specifically, the addition of 20 mm × 5 mm mask chips leads to the highest peak stress ratio (13.7 for σ_3' = 50 kPa and 8.9 for σ_3' = 100 kPa) and residual stress ratio (9.4 and 5.8). While pure sand has the smallest peak stress ratio (7.8 and 6.0) and residual stress ratio (4.4 and 3.3). The 10 mm × 10 mm mask chips yield the second highest peak stress ratio, followed by the 12 mm × 3 mm mask chips, both of which surpass the performance of pure sand.

By comparing the stress-strain curves of three types of mask chips, it can be concluded that under the same conditions, larger mask chips lead to a more significant increase in soil strength in the studied range. Additionally, test results indicate that when the area is the same, the greater the aspect ratio, the more pronounced the reinforcement effect. The findings are in agreement with (Sadek et al. 2010). This phenomenon can be explained by considering the reinforcement mechanism provided by the mask chips. The introduction of mask chips leads to strong soil-mask bonding, which enhances the integrity of the entire sample. When subjected to shearing forces, the mask chips stretch and deform, absorbing a portion of the external load and limiting the displacement of soil particles, resulting in increased strength (Xu et al. 2022; Zhao and Zheng 2022). Thus, a larger surface area of the mask chips allows for more fibers to interlock with the sand particles, creating stronger connections within the mixture. Furthermore, a higher aspect ratio of the mask chips facilitates the packing of particles, making it easier for them to arrange themselves in a more compact and stable configuration. And from the current study, the area of the mask chips seems to have a more significant impact on the strength, as the reinforcement effect of 10 mm × 10 mm mask chips is more pronounced than the 12 mm × 3 mm mask chips, despite the former having a lower aspect ratio. A plausible explanation for this phenomenon is that since the length of the chips is similar for both groups, the number of particles aligning along this dimension remains relatively constant. Therefore, it is the width that becomes a decisive factor in determining the extent of interaction between the particles and the chips. A greater width provides a larger surface area for contact and interlocking, which in turn, contributes more significantly to the strength. However, given the current limitations of the research, a more comprehensive study is needed to confirm this explanation.

Fig. 4.4 illustrates the impact of incorporating mask chips on the initial modulus (E_0) of the mixed samples. The initial modulus is determined by the ratio of deviatoric stress to axial strain, ranging from 0% to 0.1% strain in this study. The data indicates that for a constant mask chip size, increasing the lateral pressure from 50 kPa to 100 kPa leads to a significant increase in the elastic modulus, highlighting the pressure-sensitive characteristics of sand stiffness. However, integrating mask chips into the sand consistently results in a reduction in E_0 across all the lateral pressures tested. This reduction is substantial, with E_0 decreases of up to 20% for certain chip sizes; for instance, 20 mm × 5 mm chips at 50 kPa lateral pressure and 12 mm × 3 mm chips at 100 kPa show notable decreases compared to the pure sand samples. Despite these findings, the relationship between the stiffness and the sizes of mask chips is not immediately clear due to the limited scope of the experiments conducted. Future research with a broader array of experiments is essential to establish a more definitive understanding of these relationships.

Fig. 4.5 summarizes the major principal strain at the peak stress for all samples, along with the peak and residual stress differences for reference. It is noteworthy that the inclusion of mask chips not only increases the strength of the sample but also significantly postpones the peak stress. For example, under 50 kPa effective lateral pressure, the axial strain corresponding with the peak stress is 2.9% for pure sand, while the value rises to 5.5%, 6.1%, and 7.3% for the sample with 10 mm × 10 mm, 12 mm × 3 mm, and 20 mm × 5 mm mask chips, respectively. And for the 100 kPa case, the peak stress occurs at 3.8% axial strain in the pure sand sample, while the counterparts of the other three groups containing mask chips range from 6.6% to 7.4% axial strain. The observed strength enhancement and peak stress delay phenomenon are not unique to mask chips. Similar effects have been reported in triaxial or unconfining compression experimental observations when polypropylene fibers are incorporated into sand (Ganiev et al. 2022; Khodabandehlou et al. 2023). This delay in stress peak suggests an enhanced ductile behavior and improved energy absorption capacity of the sand-mask chips mixture (Zhang et al. 2022), which can be attributed to the improved interlocking and particle interaction between the mask chips and the surrounding sand particles. As a result, the sand reinforced with mask chips exhibits increased resistance to deformation and failure.

4.3.2 Strain-strain relationship

The minor principal strain ε_3 can be expressed as:

$$\varepsilon_3 = \varepsilon_v - \varepsilon_1 - \varepsilon_2 \qquad (4-2)$$

where ε_v is the volumetric strain monitored using the volume controller during the test, ε_1 is determined by the ratio of axial displacement to the sample height, and ε_2 is equal to 0 considering the plane strain conditions. Thus, ε_3 could be calculated and the evolution of ε_3 against ε_1 is shown in Fig. 4.6. Note that the positive values represent contraction while the negative ones stand for dilation.

Throughout the shearing process, the minor principal strain remains negative, indicating volumetric expansion in the direction confined by water. When the major principal strain is relatively low (below 10%), the pure sand sample exhibits a more significant dilation in minor principal strain than the sand-mask mixture sample under constant lateral pressure. It suggests the inclusion of mask chips has an inhibitory effect on volume dilation in the minor principal strain direction, which could be understood as a representation of the reinforcement effect of mask chips, i.e., restricting the particle displacement and hindering the tensile cracks, thus contributing to the overall stability of the specimen (Li et al. 2020).

Notably, the slope of the tangent line of the ε_3–ε_1 curve of the sand reinforced with the mask gradually increases when the minor principal strain is relatively low. This demonstrates that the expansion along the minor principal strain accelerates as the major principal strain increases. In contrast, in the pure sand sample, a distinct decrease in the slope could be observed when the major principal strain reaches around 5%. This change may be attributed to the formation of shear bands, which will be discussed in the subsequent section. Once the major principal strain reaches 10%, the slope remains almost constant, indicating both the pure sand and the reinforced sand maintain a very close expansion rate.

Moreover, the comparison between Fig. 4.6(a) and Fig. 4.6(b) shows a lower lateral pressure leads to a larger minor principal strain corresponding to the same major principal strain in the same sample, promoting sample dilation. Fig. **4.9** displays the photos of the sample taken after shearing. Visual inspections corroborate the quantitative findings, showing that as the axial strain develops, the sample gradually expands in the direction perpendicular to the glass plates until failure.

The deviatoric strain ε_d can be determined by

$$\varepsilon_d = \frac{\sqrt{2}}{3}\sqrt{(\varepsilon_1 - \varepsilon_2)^2 + (\varepsilon_1 - \varepsilon_3)^2 + (\varepsilon_2 - \varepsilon_3)^2} \qquad (4-3)$$

Fig. 4.7 displays the volumetric strain-deviatoric strain relationship. All samples exhibit a contractive phase followed by a dilative phase of the volume. During the initial shearing stage, the samples are compressed in volume, with sand-mask mixtures exhibiting greater compressibility. One possible explanation is that the presence of mask chips might cause a change in the particle arrangement and packing (Madhusudhan et al. 2017). During the shearing process, the sand-mask mixture could undergo a more significant particle rearrangement to achieve a more stable configuration, leading to higher contraction strain. In addition, the mask chips may inevitably overlap when preparing the sample, which could create localized areas with higher compressibility. After the contractive volume strain reaches the peak, it gradually decreases to zero due to the rearrangement of soil particles and mask chips within the sample, and subsequently exhibits dilation.

Fig. 4.8 provides a summary of the cumulative contractive and dilative volumetric strain across all samples. The experimental results indicate that as mask chips area increase, a more noticeable cumulative dilation occurs in the mixture specimen. A plausible explanation for this could be that a larger mask-chip area facilitates greater interlocking between particles, particularly as shearing advances. This interlocking can resist the tendency for particles to slide past each other easily, resulting in a more pronounced dilative behavior when the sample expands in volume to accommodate shear deformation. However, it is important to note that current literature lacks consensus regarding the influence of fibers on the volumetric response of the soil. Determining whether fibers impede or enhance compression or dilation is challenging, as a variety of factors can impact the volumetric response, including test methods, confining pressure, soil properties (initial void ratio, soil type), and fiber properties (content, aspect ratio). Consequently, different studies may yield inconsistent or even contradictory findings. For instance, Santos et al. (Dos Santos et al. 2010) discovered that, at a lateral pressure of 100 kPa, polypropylene fibers increased the initial compression of quarzitic sand while inhibiting subsequent dilation in triaxial tests, with minimal effects observed at higher stress levels. Conversely, Silveria et al. (Silveira et al. 2021) reported that polypropylene fibers significantly reduced the contraction tendency of clay in direct shear tests. Additionally, Wood et al. (Muir Wood et al. 2016) demonstrated that incorporating polypropylene fibers led to a more dilative volumetric response of sand, as evidenced by both direct shear tests and numerical simulations. In conclusion, the diverse outcomes of these studies underscore the necessity for further detailed micro-structural investigations or advanced numerical simulations to establish a comprehensive understanding of the complex interplay between mask chips and soil volumetric response.

4.3.3 Shear band characteristics

Shear bands refer to the concentration of deformation within narrow planes of intensely sheared material. In this experiment, two distinct shapes of shear bands in the specimens have been observed through the glass plates, i.e., a simple linear form and a more complex X-shaped pattern (Fig. **4.9**). The simple shear bands appeared as individual, straight lines within the sample, whereas the X-shaped shear bands were characterized by the intersection of two linear shear bands, forming a distinct X pattern.

The inclination angle of shear bands is critical in predicting failure planes in soils. Comparing theoretical and measured values allows for the assessment of the accuracy of current theory models under various stress states, confining pressures, and material properties. Discrepancies between theory and measurements may suggest that the theoretical model does not fully capture the complexity of the mask-sand behavior, leading to improvements in design and construction practices. The conventional approaches for determining the angle of inclination of shear bands in frictional materials subjected to plane strain are known as the Mohr-Coulomb solution, the Roscoe solution, and the Arthur solution (Alshibli Khalid and Sture 2000). The inclination angle of the shear band based on the Mohr-Coulomb criterion is as:

$$\theta_C = 45° + \frac{\Phi_m}{2} \qquad (4-4)$$

where θ_C is the angle measured from the direction of the minimum principal effective stress, and Φ_m is the mobilized angle of internal friction.

The inclination angle given by Roscoe (Roscoe 1970) can be expressed as

$$\theta_R = 45° + \frac{\Psi_f}{2} \qquad (4-5)$$

where θ_R is the angle between the direction of the minor principal strain increment $d\varepsilon_3$ and Ψ_f is the angle of dilation at failure.

Arthur (Arthur et al. 1977) proposed another expression based on the experimental observations as

$$\theta_A = 45° + \frac{\Phi_m + \Psi_f}{4} = \frac{1}{2}(\theta_C + \theta_R) \qquad (4-6)$$

In this study, the theoretical shear band inclination angle was calculated based on Eq. (4)-(6), and the measured shear band inclination angle was obtained with the help of the membrane with grids. The results are listed in Table 4.2. The theoretically predicted inclination angle of the shear band is within the range of 50 to 60 degrees, overestimating the inclination angle compared with experimentally measured values (45-55 degrees at 15% major principal strain). Among all the theories, the results obtained using the Roscoe method provide the closest correspondence. And in general, the inclination angle decreases as the effective lateral pressure rises.

Shear bands are not simply two-dimensional planes of slippage; instead, they are three-dimensional regions where deformation is concentrated. The measurement values of shear band thickness are also shown in Table 4.2. In this study, the observed shear band typically falls within the 12 mm to 14 mm range, around 15 and 18 times the median particle size (d_{50}), which is consistent with the range of 10 to 30 times reported in previous research (Kuhn 2017; Rattez et al. 2022). Apart from particle size, lateral pressure also plays a role in determining shear band thickness. As lateral pressure rises, the shear band gets thinner, provided other factors remain constant. It could be understood that higher lateral pressure restricts the dilation of the specimen, resulting in a more uniform stress distribution and a thinner shear band (Gu et al. 2014). However, no obvious correlation is observed between mask chip inclusion and the shear band thickness based on the limited experiments in this study.

The formation of shear bands is a gradual process that includes the initiation, development, and final complete formation of the shear band. With the help of the video camera and the membrane with grids, the development of the shear band was monitored during the deformation process. Fig. 4.10 shows the typical development of shear bands and corresponding stress-strain relationships during the shearing process for samples of pure sand and sand with 12 mm × 3 mm mask chips. Three stages of shear deformation are displayed, corresponding to before peak stress, peak stress, and after peak stress, respectively. Taking the case of sand with 12 mm × 3 mm mask chips as an example, during the stage where the stress difference increases (point D), local deformation can be observed in the image. When the stress reaches the peak value, slight deformation can be observed along the diagonal direction, but the shape of the shear band is not clear yet. At the point where the stress drops to the residual value (point F), a single linear shear band is fully developed and can be clearly observed. The situation is similar for pure sand. The observations agree with the findings both in experiments and numerical simulations (Wu et al. 2020; Wu et al. 2017). In summary, the development of shear bands initializes before peak stress and forms after peak stress.

4.4 Discussions

In this study, the impact of mask chip dimensions on soil reinforcement has been investigated by selecting three distinct mask chip sizes: 20 mm × 5 mm, 10 mm × 10 mm, and 12 mm × 3 mm. These sizes were specifically chosen to examine the influence of both the mask chips area and their aspect ratio. To facilitate a standardized comparative analysis, a dimensionless parameter, denoted as η, was introduced to encapsulate the relationship between the mask chip dimensions and the mean diameter of the soil grains. The parameter is defined as follows:

$$\eta = \frac{L_x}{D_{50}} + \frac{L_y}{D_{50}} = \frac{L_x + L_y}{D_{50}} \qquad (4-7)$$

where L_x and L_y stand for the width and length of the mask chips, respectively, and D_{50} is the mean diameter of the tested sand. The η values for the mask chips with dimensions of 20 mm × 5 mm, 10 mm × 10 mm, and 12 mm × 3 mm were calculated to be 32.1, 25.7, and 19.3, respectively. An η value of 0 was assumed for pure sand, serving as a control benchmark for comparison.

The correlation between the enhancement of soil strength using mask-reinforced sand and the calculated η values is depicted in Fig. **4**.**11**. The strength ratio in this figure is defined as the ratio of the peak or residual stress in mask-reinforced sand samples to the corresponding stress measured in pure sand. Analysis of the figure reveals a consistent pattern: a larger η value generally leads to an improvement in strength. Specifically, the mask chips with the highest η value of 32.1 (20 mm × 5 mm) exhibited a considerable improvement in strength ratio at both lateral pressure levels, highlighting the significance of the dimensionless parameter in the soil reinforcement process. Moreover, the assessment of residual stress supports these findings, except for one outlier. This trend suggests that samples with higher η values are inclined to sustain elevated residual stresses, indicating a durable reinforcement effect.

Overall, at least in this study, the introduction of the η coefficient enables a systematic assessment of the impact of mask chips on soil behavior, considering both their length and width in a simple and intuitive manner. Future research will expand the scope of this study by incorporating additional mask chip dimensions to further evaluate the potential of η as a predictive parameter in geotechnical applications, especially for soils reinforced with a broader range of mask chip sizes.

4.5 Summary

In the present study, a series of biaxial compression tests were conducted to explore the mechanical behavior of the mask-chips-reinforced sand. Three various sizes (20 mm × 5 mm, 10 mm × 10 mm, and 12 mm × 3 mm) of mask chips were added to dense sand samples at the mass ratio of 0.5%, with pure sand as a reference. The stress-strain and strain-strain relationships during shearing under different effective pressures (50 kPa and 100 kPa) were analyzed. And the development of the shear band was monitored using a video camera.

The study concluded that the inclusion of mask chips enhances the strength and delays the stress peak, with 20 mm × 5 mm chips showing the best reinforcement performance. The strain corresponding to the peak stress also increased with the presence of mask chips. The mask-chips-reinforced sand underwent greater compression during the contraction stage, which could be due to changes in particle arrangement and packing. Two distinct shear band shapes were observed, with the mask chips playing an insignificant role in their formation. The dimensionless parameter η correlated the mask chip size and mean diameter of the grain particles, indicating a positive correlation between strength improvement and this parameter.

These findings contribute to a better understanding of the mechanical behavior of sand reinforced with mask chips, offering potential applications in ground improvement and geotechnical engineering. Additionally, it addresses the important matter of recycling and reusing disposable masks. Future research could focus on various relative densities of the sand, cyclic loadings, and long-term performance to further optimize the reinforcement properties. However, the need to customize mask dimensions introduces additional processing costs, adding an economic aspect to the methodology. Therefore, careful consideration and balance of these factors are crucial for the successful implementation of this approach.

Table 4.1 Physical parameters of tested sand

Parameters	Value
Maximum particle size, d_{max} (mm)	1.18
Minimum particle size, d_{min} (mm)	0.60
Median particle size, d_{50} (mm)	0.78
Coefficient of uniformity, C_u	1.28
Specific gravity, G_s	2.65
Maximum void ratio, e_{max}	0.81
Minimum void ratio, e_{min}	0.56

Table 4.2 Comparison of theoretical shear band inclination angle and experimental measurements including thickness

Samples	$\sigma_3'^{a}$ (kPa)	$\theta_C{}^{b}$ (°)	$\theta_R{}^{c}$ (°)	$\theta_A{}^{d}$ (°)	$\theta_M{}^{e}$ (°)	d^{f} (mm)
sand	50	63.0	56.9	60.0	55	14
	100		57.0	60.0	50	12
10 × 10	50	61.5	54.5	58.0	51	14
	100		51.4	56.5	45	12
20 × 5	50	64.0	52.2	58.1	51	13
	100		51.5	57.9	50	12
12 × 3	50	57.5	51.8	54.6	52	14
	100		51.1	54.3	48	12

a. Effective lateral pressure
b. Coulomb shear band inclination angle
c. Roscoe shear band inclination angle
d. Arthur shear band inclination angle
e. Measurement values of shear band inclination angle
f. Thickness of shear band

Fig. 4.1 Tested sample preparation, including tested sand microscope camera photo, grain distribution curve, and masks

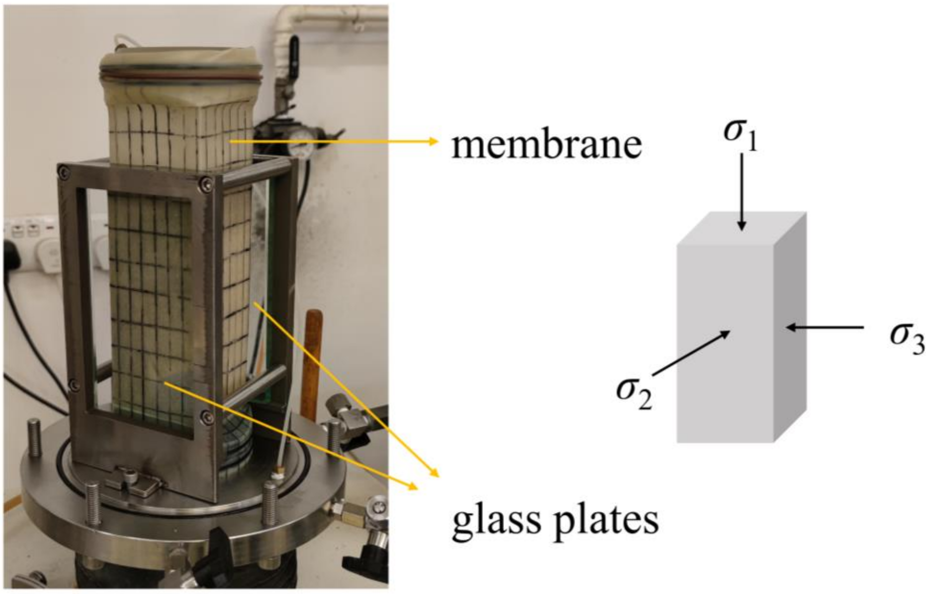

Fig. 4.2 Biaxial compression sample set-up and sketch map

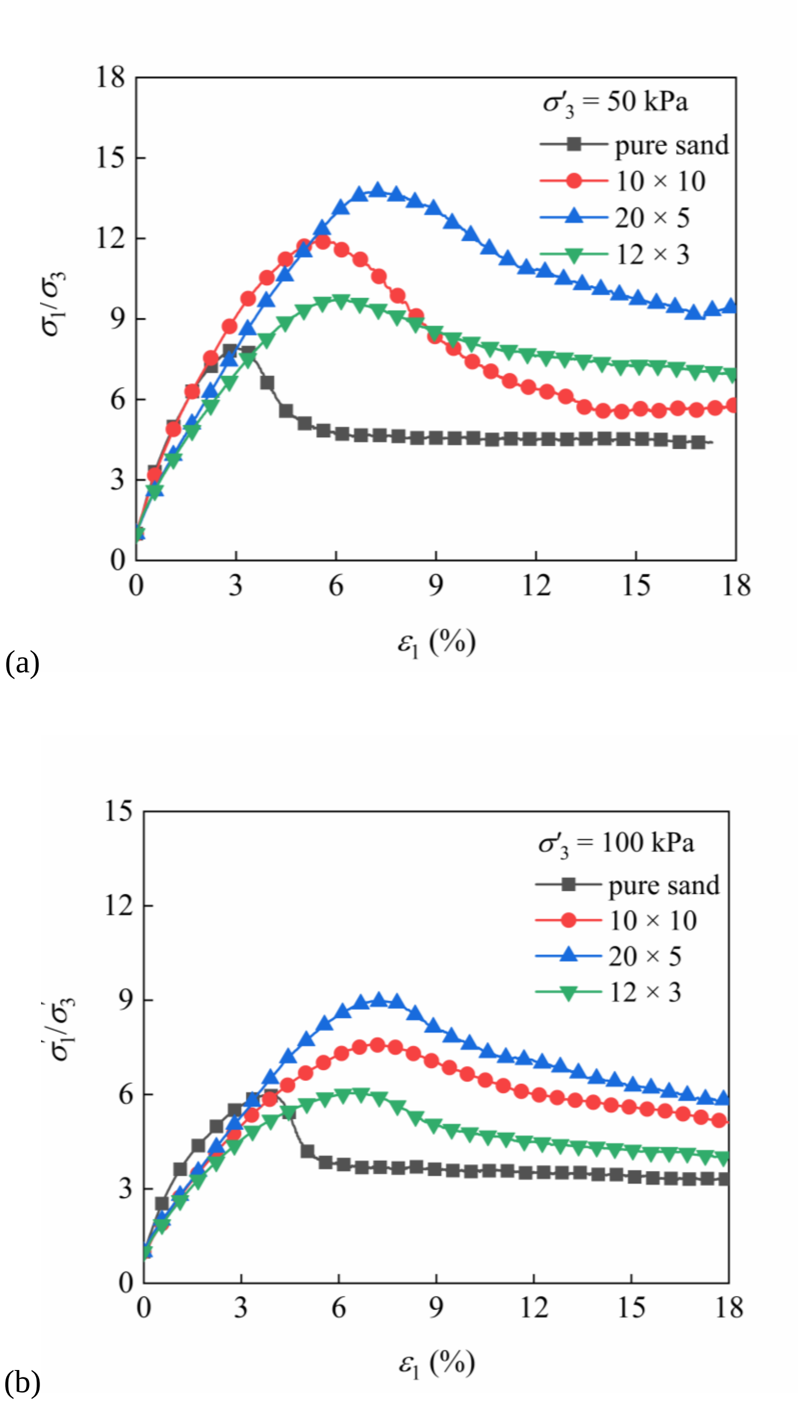

Fig. 4.3 Principal stress ratio ($\boldsymbol{\sigma'_1/\sigma'_3}$) for different groups under (a) 50 kPa and (b) 100 kPa effective lateral pressure

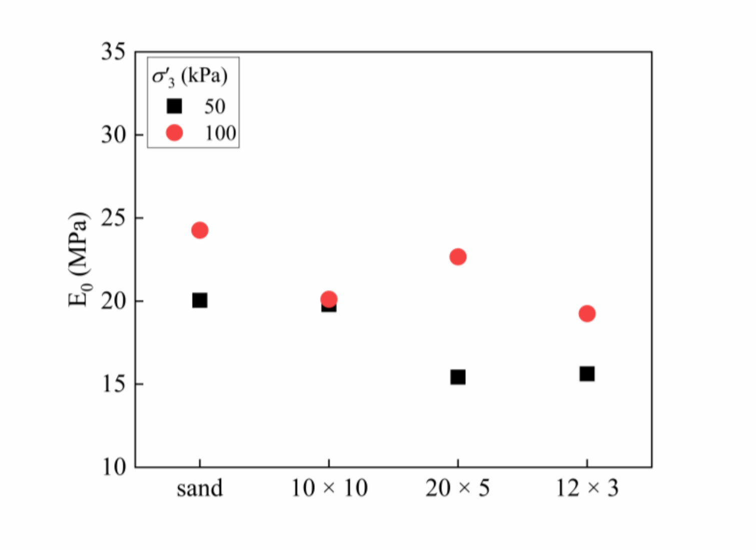

Fig. 4.4 Initial elastic modulus (E_0) calculated for different groups under 50 kPa and 100 kPa effective lateral pressure

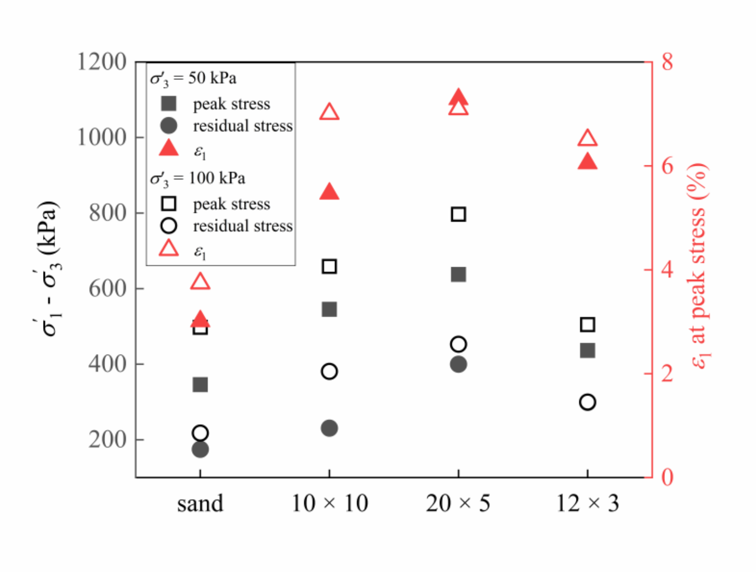

Fig. 4.5 Peak and residual stress differences ($\sigma_1' - \sigma_3'$) and major principal strain (ε_1) at peak stress for different groups under 50 kPa and 100 kPa effective lateral pressure

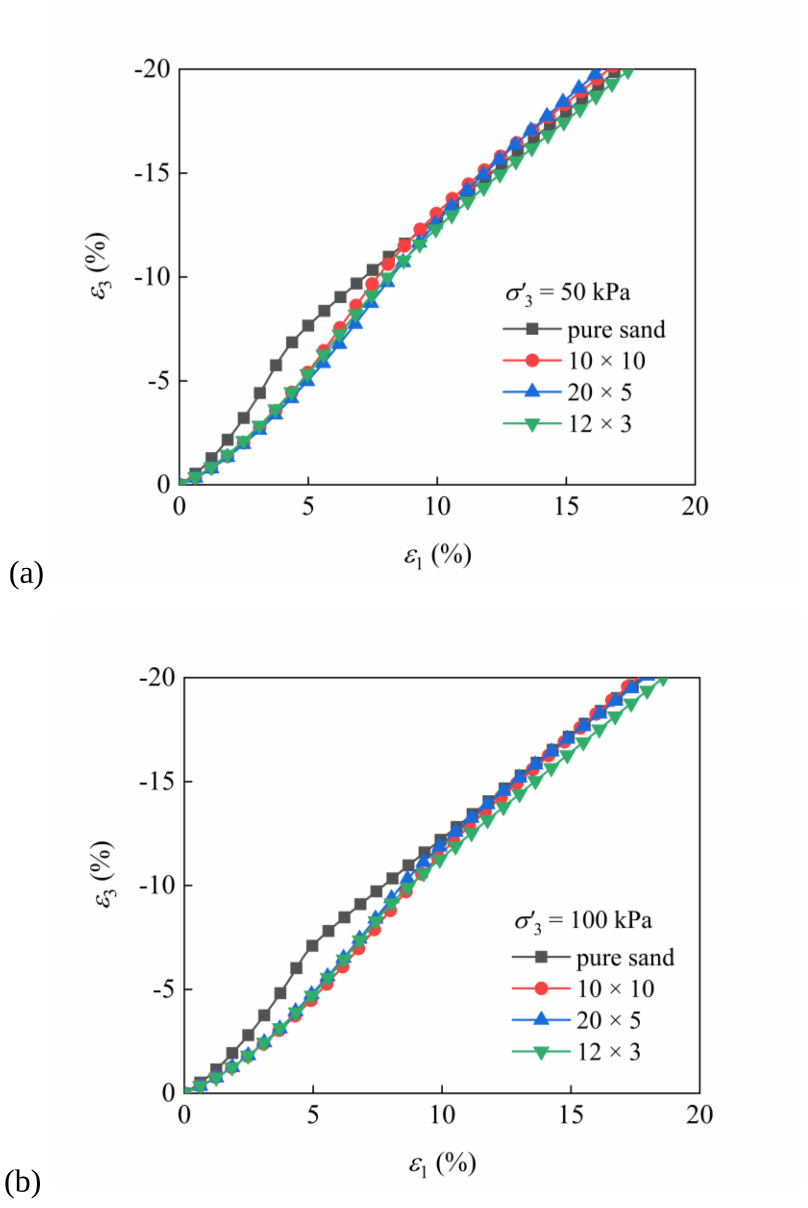

Fig. 4.6 Relationship between minor principal strain (ε_3) and major principal strain (ε_1) during shearing for different groups under (a) 50 kPa and (b) 100 kPa effective lateral pressure

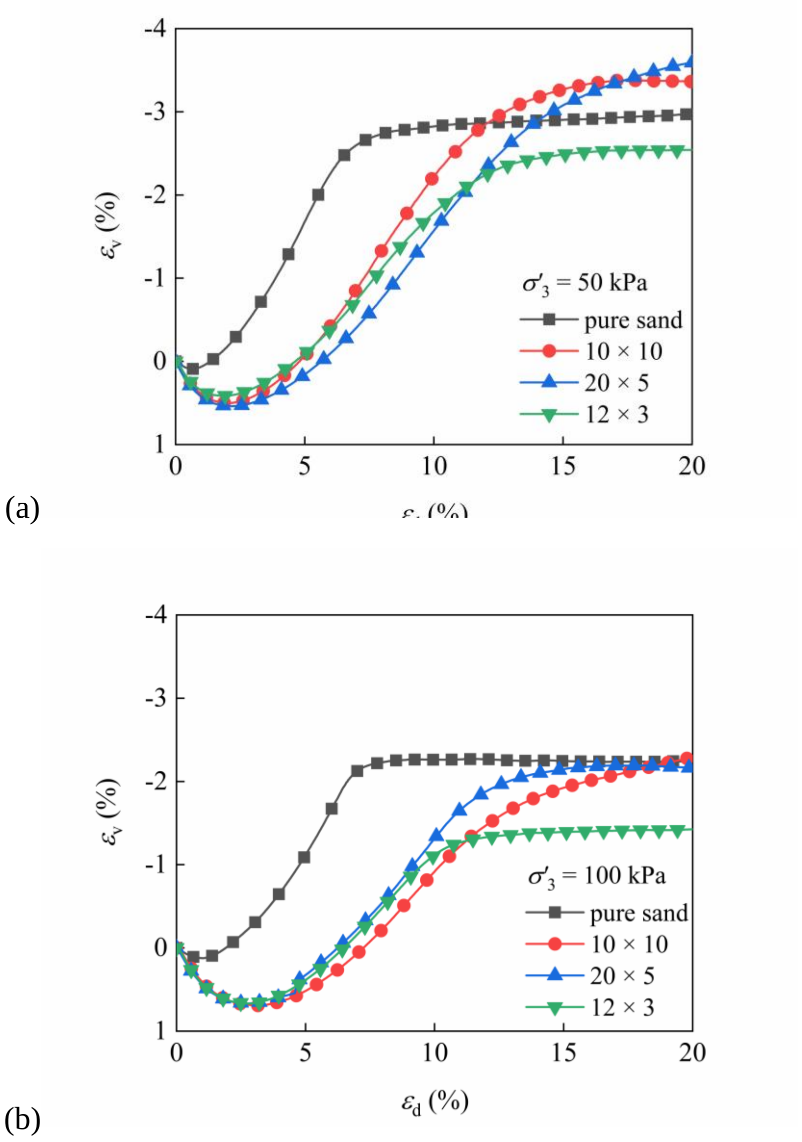

Fig. 4.7 Relationship between volumetric strain (ε_v) and deviatoric strain (ε_d) during shearing for different groups under (a) 50 kPa and (b) 100 kPa effective lateral pressure

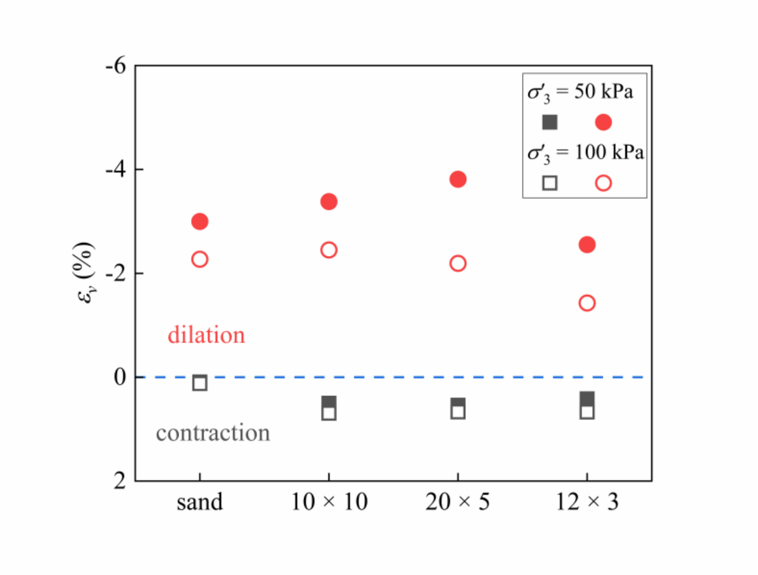

Fig. 4.8 Cumulative contractive and dilative volumetric strain for different groups under 50 kPa and 100 kPa effective lateral pressure

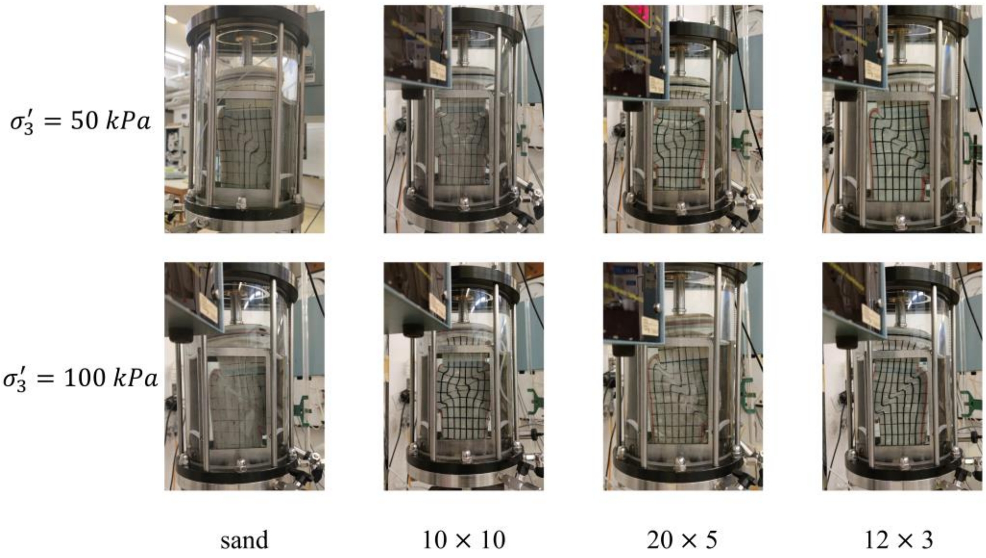

Fig. 4.9 **Various shear band types**

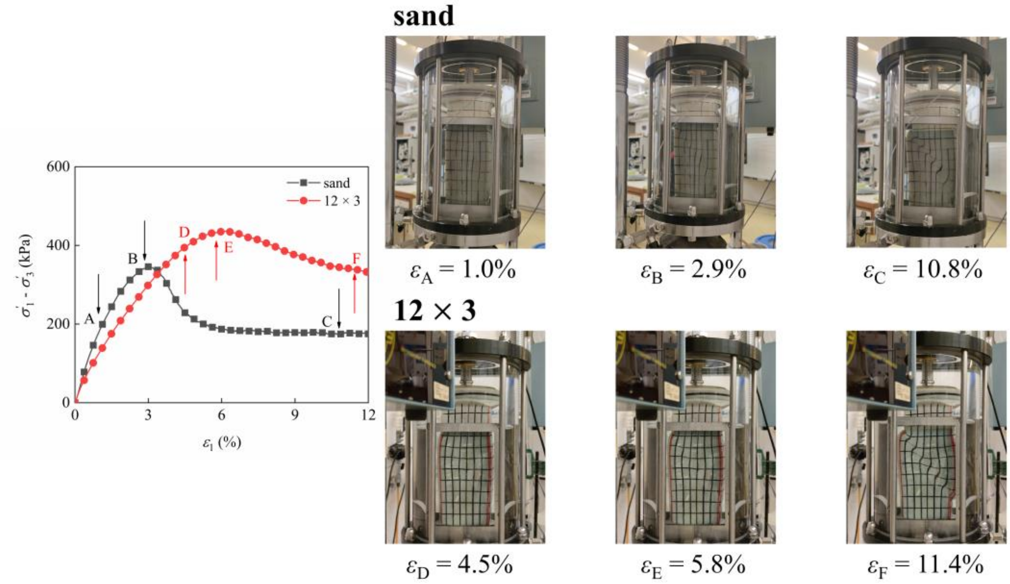

Fig. 4.10 Stress differences evolution against major principal strain during shearing and corresponding visual views of the sample of pure sand and containing 12 mm × 3 mm mask chips ($\sigma_3' = 50\ kPa$)

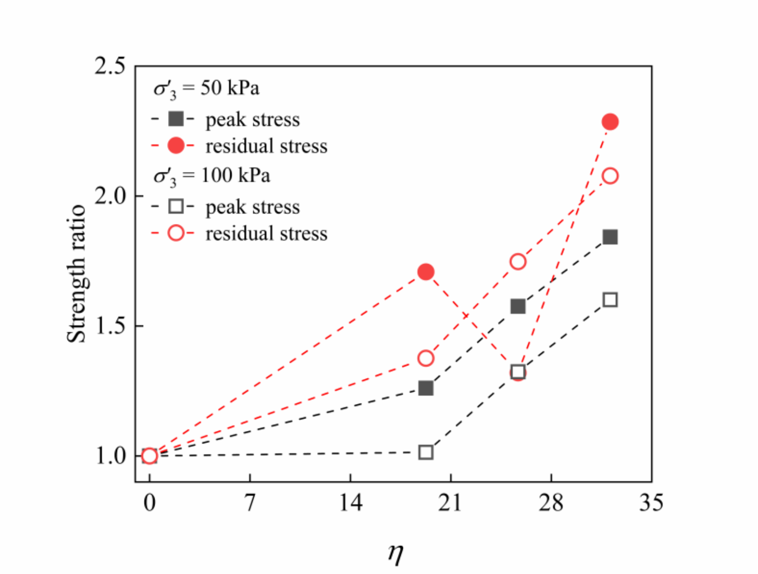

Fig. 4.11 The relationship between the enhancement of soil strength using mask-reinforced sand and the calculated η values

Chapter 5 An Elastoplastic Constitutive Model for Mask Chips-Granular Soil Mixture

5.1 Introduction

Soil reinforcement using different additives has been widely developed in geotechnical fields to enhance the engineering performance of soil structures. Those additives traditionally include materials such as cement, limes, geotextiles, plant roots, flex fibers, etc. In recent years, disposable masks have grown in popularity as an alternative additive to traditional materials (Tang et al., 2020; Saberian et al., 2021; ur Rehman and Khalid, 2021; Zhang et al., 2022). The reasons can be attributed to (1) due to the outbreak of COVID-19, the extensive use of disposable masks has caused significant environmental challenges (Dhawan et al., 2019; Fadare and Okoffo, 2020; Zand and Heir, 2020); therefore, using disposable masks as reinforcement material can reduce environmental pollution and conserve resources, and (2) disposable masks are flexible materials that can effectively enhance the overall strength of soil without causing brittle failure (Saberian et al., 2021; ur Rehman and Khalid, 2021). Therefore, an in-depth study of the mechanical behavior of mask chips granular soil mixture (MSM) is of great significance to promote the application of disposable masks in engineering practice and protect the environment.

Because mask chips are composed of polypropylene fibers, MSM is a kind of fiber-reinforced soil in essence. Although the predecessors have conducted a lot of research work on the mechanical behavior of fiber-reinforced soil, the stress strain characteristics of fiber-reinforced soil are closely related to materials (Lee et al., 2014; Mashiri et al., 2016; Fathali et al., 2017; Qi et al., 2018). The results obtained for the fibers with other chemical compositions and structural forms are not completely applicable to MSM. Previous researchers have also conducted some research on the mechanical behavior of MSM. Based on discussing the role of environmental geotechnics in reducing the impact of epidemic diseases, Tang et al. (2020) believed that disinfected medical waste (such as mask chips) could be used in geotechnical engineering. Saberian et al. (2021) conducted a series of mechanical tests on recycled concrete aggregate with different proportions of mask chips, and found that mask chips could improve the strength, stiffness, ductility, and flexibility of recycled concrete aggregate. ur Rehman and Khalid (2021) combined the use of mask chips and silica fume to improve the mechanical properties of clay, and pointed out that mask chips could not only improve the strength of clay, but also regulate the ductility and deformability. Zhang et al. (2022) conducted a series of monotonic and cyclic triaxial shear tests on MSM under different conditions and found that mask chips could improve the strength of granular soil and reduce the dilatancy. Ghadr et al. (2022) studied the effects of the weight fraction of mask chips, the length of mask chips, and the initial mean effective stress on the undrained shear behavior of sand. It was found that MSM has dilatancy and strain-hardening behavior, and the stress ratio and friction angle of MSM increased with the increasing mask chip length. Xu et al. (2022) revealed the influence of the mask chips content on the strength characteristics of complete decomposed granite and found that under the effective confining pressure of 120 kPa, the shear strength of complete decomposed granite increased the most when the volume content of mask chips was 0.5%. Wang et al. (2022) proposed using the mask chips as an additive for hot mix asphalt to improve rutting resistance. In conclusion, although predecessors have achieved rich research results in the mechanical behavior of MSM, a constitutive model suitable for MSM has not yet been proposed. Studying the constitutive model of MSM is the premise for using it to conduct engineering construction activities. Therefore, it is crucial to build a constitutive model that can reasonably describe the stress strain relationship of MSM.

The present work aims to propose a constitutive model for predicting the mechanical behaviors of MSM and provides theoretical guidance for its engineering applications. First, the mechanical characteristics of MSM are investigated by a series of laboratory tests. Furthermore, based on the critical state theory, a state-dependent elastoplastic constitutive model for MSM is established using the non-associated flow rule. In addition, the model is validated by conventional triaxial shear tests on both pure sands and mask chips reinforced sands under various loading conditions. The comparison results demonstrate the proposed model can model the variation of strength, stiffness, and dilatancy of soil induced by mask chips.

5.2 Experimental observation of MSM

5.2.1 Materials, sample preparation, and testing program

We first conducted a series of consolidation-drained triaxial shear tests to investigate the reinforcing effect of mask chips when mixed with pure sand. The tested sand was Fujian standard sand, commonly used in geotechnical laboratory tests in China. To ensure accurate comparisons, only grains with a particle size between 0.60 mm –1.18 mm was selected for testing. The mask chip used in this study is a polypropylene-based material with low density and good fatigue resistance. One can refer to our previous work by Zhang et al. (2022) for more detailed descriptions of the mask. In the tests, the mask chips were randomly incorporated into sands to create MSM samples, which present a cylindrical shape with a diameter of 100 mm and a height of 200 mm. The MSM samples included three mask chip dimensions: 10 mm × 10 mm, 12 mm × 3 mm, and 20 mm × 5 mm. These samples were labeled as MSM-I, MSM-II, and MSM-III, respectively. The mass ratio of mask chips to the granular soil in each MSM was 0.5%. Table **5.1** provides an overview of the main physical parameters for both pure sand and the MSM samples.

The mechanical behavior of MSM was further investigated by consolidation-drained triaxial shear tests under various effective confining pressures (σ_3'=50, 100, and 200 kPa) and relative densities (D_r = 60% and 90%). These tests were performed with a constant shear rate of 0.6 mm/min in axial strain. Once the axial strain reached 20%, the tests were terminated.

5.2.2 Strength and deformation characteristics of MSM

Furthermore, we will investigate the mechanical response of MSM based on the experimental results. Note that in this section, only the experiment with $D_r = 90\%$ under the effective confining pressure of 100 kPa is used for our investigation. The test results under effective confining pressures of 50 kPa and 200 kPa will be employed for our model validation in Section 4. Fig. 5.1(a) and (b) present the experimental deviatoric stress axial strain and volumetric strain axial strain curves of pure sand and MSMs with an identical relative density of $D_r = 90\%$. The MSMs show significantly higher peak strength and smaller dilatancy compared to pure sand. Additionally, the initial stiffness of sand is noticeably reduced, while the critical strength is enhanced after reinforcing with mask chips. This contrasts with the experimental results of fiber-reinforced sand (Diambra et al., 2013), where the initial stiffness increases with fiber contents. The reason can be attributed to the fact that the mask chip is a very soft material that cannot withstand significant pressure within a small range of deformation. However, as the loading progresses, the mask chip starts to contribute its tensile strength once the axial strain exceeds a certain range. As a result, the overall strength of the sand is enhanced. Moreover, the aspect ratio of the mask chip can affect the shear strength of MSM. Among the MSM samples with three different aspect ratios, MSM-III exhibits the highest strength, while MSM-I shows the lowest strength. This indicates that a strip-shaped mask chip is more likely to demonstrate better tensile performance in sands.

The above experimental study indicates that the MSM has the following mechanical features compared to pure sand: (1) The MSM shows higher peak strength and smaller dilatancy. (2) The MSM exhibits smaller initial stiffness. (3) The MSM demonstrates higher strength at the critical state. These features will contribute to the development of our constitutive model for MSM.

5.2.3 Critical state of MSM

Fig. **5**.**2**(a) illustrates the critical state lines in the *e*–In*p* plane for pure sand, MSM-I, MSM-II, and MSM-III, with a relative density of 90%. The results show that the critical state lines of the three MSM samples are approximately parallel to those of pure sand. Generally, the critical state line of MSM is located lower than that of pure sand, which aligns with the experimental observations made by Gao and Zhao (2020). This can be attributed to the fact that the mask chip can reduce the deformation of sands, thereby reducing the dilatancy and resulting in an overall decrease in the critical void ratio.

Fig. **5**.**2**(b) presents the critical state lines in the *p*–*q* plane for pure sand, MSM-I, MSM-II, and MSM-III with relative densities of 90%. It can be observed that the critical state lines of all the MSM samples are approximately parallel to that of pure sand. However, the intercept of each MSM critical state line is significantly larger than that of pure sand. This indicates that the mask chips can contribute tensile strength to the MSM even under a critical state, which is consistent with the conclusions of Zaimoglu and Yetimoglu (2012) and Anagnostopoulos et al. (2014). Moreover, this enhanced tensile strength may lead to a notable strain-hardening effect in the MSM, as mentioned by Machado et al. (2008). These observations highlight the influence of mask chips on the critical state of the MSM and serve as a foundation for our subsequent model construction.

5.3 Constitutive model for MSM

In this section, a constitutive model for MSM based on the experimental observation in Section 2 is developed. The SIMSAND model proposed by Yin (2021) is referenced for our development. This model is a simple critical state-based nonlinear model within the framework of elastoplastic. It requires 11 parameters and can well describe the stress dilatancy and state-dependency of granular soils. One can refer (Yin et al., 2016, 2018) for more details. In the present work, to consider the tensile strength induced by mask chips, an additional parameter (p_R) is introduced to modify the yield condition, plastic potential, and plastic strain increment, as well as the critical state of the reference model.

5.3.1 Yield surface

The yield surface of the reference model can be expressed as

$$f = \frac{q}{p} - \frac{M_p \varepsilon_d^p}{k_p + \varepsilon_d^p} \tag{5-1}$$

where q is the deviatoric stress. p is the mean effective stress. M_p is the peak stress ratio. k_p relates to the plastic shear modulus. ε_d^p is the deviatoric plastic strain ($\varepsilon_d^p = \sqrt{2e_{ij}e_{ij}/3}$).

According to the experimental results (Fig. 5.1), the effect of mask chips on MSM can be regarded as an additional tensile strength. Therefore, a modified mean effective stress is proposed in this study, and the yield surface can be modified as:

$$f = \frac{q}{p + p_R} - \frac{M_p \varepsilon_d^p}{k_p + \varepsilon_d^p} \tag{5-2}$$

where p_R denotes the tensile strength caused by mask chips.

5.3.2 Plastic potential

Accordingly, the stress dilatancy relationship for MSM can be updated as:

$$\frac{d\varepsilon_v^p}{d\varepsilon_d^p} = A_d \left(M_{pt} - \frac{q}{p + p_R} \right) \tag{5-3}$$

where $d\varepsilon_v^p$ and $d\varepsilon_d^p$ are plastic volume strain and plastic shear strain increments, respectively. A_d controls the magnitude of dilatancy. M_{pt} is phase-transformation stress ratio. Specifically, in the case of M_{pt} greater than the current stress ratio, the soil undergoes contraction; conversely, dilatancy occurs.

Moreover, experimental studies have shown that there is a small elastic region for granular soils, especially when the stress ratio is very small. This indicates that the undrained stress path in the q–p plane is generally perpendicular to the p-axis at the beginning of loading. Therefore, to improve the undrained prediction, the parameter A_d can be modified as follows:

$$A'_d = \left[1 - exp\left(-A_d \frac{q}{p+p_R}\right)\right] \tag{5-4}$$

As a result, the partial derivatives of the plastic potential function (g) for p and q can be expressed as follows by using the non-associated flow rule (Yin et al., 2018):

$$\frac{\partial g}{\partial p} = A'_d \left(M_{pt} - \frac{q}{p+p_R}\right) \tag{5-5}$$

$$\frac{\partial g}{\partial q} = 1 \tag{5-6}$$

5.3.3 Elastic-plastic strain increment

In the p–q plane, the total strain increment can be decomposed into elastic and plastic parts:

$$\begin{cases} d\varepsilon_v = d\varepsilon_v^e + d\varepsilon_v^p \\ d\varepsilon_d = d\varepsilon_d^e + d\varepsilon_d^p \end{cases} \tag{5-7}$$

where $d\varepsilon_v$, $d\varepsilon_v^e$, and $d\varepsilon_v^p$ are the total volume strain increment, elastic volume strain increment, and plastic volume strain increment, respectively. $d\varepsilon_d$, $d\varepsilon_d^e$, and $d\varepsilon_d^p$ are the total shear strain increment, elastic shear strain increment, and plastic shear strain increment, respectively.

The elastic strain increment can be expressed as:

$$\begin{cases} d\varepsilon_v^e = \frac{dp}{K} \\ d\varepsilon_d^e = \frac{dq}{3G} \end{cases} \tag{5-8}$$

where K and G are the bulk modulus and shear modulus, respectively. To introduce the dependency of the elastic stiffness on the density and the mean effective stress, as well as the tensile strength of MSM, the bulk modulus (K) and shear modulus (G) can be extended as:

$$\begin{cases} K = K_0 p_{at} \frac{(2.97-e)^2}{(1+e)} \left(\frac{p+p_R}{p_{at}}\right)^n \\ G = G_0 p_{at} \frac{(2.97-e)^2}{(1+e)} \left(\frac{p+p_R}{p_{at}}\right)^n \end{cases} \tag{5-9}$$

where K_0 and G_0 are dimensionless reference values of bulk modulus and shear modulus, respectively. p_{at} is the standard atmospheric pressure, which is generally 101.3 kPa. e is the void ratio. n is an input parameter controlling the nonlinearity of the stress level and cohesion effects.

The plastic strain increment is determined by the flow rule, which can be expressed as:

$$\begin{cases} d\varepsilon_v^p = d\lambda \frac{\partial g}{\partial p} \\ d\varepsilon_d^p = d\lambda \frac{\partial g}{\partial q} \end{cases} \tag{5-10}$$

where $d\lambda$ is a plastic multiplier, which can be derived by:

$$d\lambda = \frac{\left[\frac{\partial f}{\partial \sigma_{ij}}\right]^T D_{ijkl} d\varepsilon_{kl}}{\left[\frac{\partial f}{\partial \sigma_{ij}}\right]^T D_{ijkl} \frac{\partial g}{\partial \sigma_{kl}} - \frac{\partial f}{\partial \varepsilon_d^p} \frac{\partial g}{\partial q}} \tag{5-11}$$

where the superscript T is a transposition operator, and D_{ijkl} is an elastic stiffness tensor.

5.3.4 Critical state line

The critical state line (CSL) proposed by Gudehus (1997) can be expressed as:

$$e_c = e_{ref} exp\left[-\lambda \left(\frac{p}{p_{ref}}\right)^{\xi}\right] \tag{5-12}$$

where e_c is the critical void ratio. e_{ref} means the initial critical void ratio. λ and ξ control the evolution rate of the CSL in the e–ln$p$ plane. Eq.(12) can solve the numerical problem that the critical void ratio may be negative at a high stress level (Yin, 2021).

However, Eq.(12) does not consider the effect of mask chips on the tensile strength of MSM. In the present work, the tensile strength reflects the effect of mask chips is incorporated in the following way:

$$e_c = e_{ref} exp\left[-\lambda \left(\frac{p+p_R}{p_{ref}}\right)^{\xi}\right] \tag{5-13}$$

Moreover, the mechanical behavior of granular soils is closely related to their current state (Li et al., 1999). To establish a state-dependent constitutive model, the state parameter (ψ) proposed by Biarez and Hicher (1994) is introduced:

$$\psi = \frac{e}{e_c} \tag{5-14}$$

Equation (14) implies $e_c/e < 1$ for loose packing, $e_c/e > 1$ for dense packing, and $e_c/e = 1$ when the initial state lies on the CSL. In this way, the relative relationship between the current state and the critical state of granular materials can be evaluated. According to Biarez and Hicher (1994), the effect of initial density on the mechanical behavior of granular soils can be considered in the model in the following way:

$$\varphi_p = \tan^{-1}(\psi^{-n_p} \tan \varphi_c) \tag{5-15}$$

$$\varphi_{pt} = \tan^{-1}(\psi^{n_d} \tan \varphi_c) \tag{5-16}$$

where φ_p, φ_{pt}, and φ_c are the peak friction angle, the phase-transformation friction angle, and the critical friction angle, respectively. The n_p and n_d are model parameters reflecting the effect of particle interlocking. Subsequently, the peak stress ratio (M_p) and the phase-transformation stress ratio (M_{pt}) can be written as:

$$\begin{cases} M_p = \frac{6 \sin \varphi_p}{3 - \sin \varphi_p} \\ M_{pt} = \frac{6 \sin \varphi_{pt}}{3 - \sin \varphi_{pt}} \end{cases} \tag{5-17}$$

5.4 Model performance

5.4.1 Summary of model parameters

The proposed constitutive model requires 12 parameters, including three elastic parameters, four critical state-related parameters, four plastic shear parameters, and one added parameter (p_R). These parameters have the following physical meanings:

(1) Elastic parameters: G_0, K_0, and n. G_0 and K_0 are dimensionless reference values of bulk modulus and shear modulus, respectively. n controls the nonlinearity of the

stress level and cohesion effect. All of them can be obtained by isotropic compression tests. Generally, we use Poisson's ratio (ν) to represent K_0 by $K_0 = 2G_0(1+\nu)/3(1-2\nu)$.

(2) Critical state parameters: e_{ref}, λ, ζ, and φ_c. e_{ref} means the initial critical void ratio. λ and ξ control the evolution rate of the CSL in the e–ln$p$ plane. φ_c is the critical friction angle. The parameter e_{ref}, λ, and ζ can be determined by isotropic compression tests. The parameter φ_c can be determined by triaxial shear tests.

(3) Plastic shear parameters: k_p, A_d, n_p, and n_d. k_p relates to the plastic shear modulus. A_d controls the magnitude of dilatancy. n_p and n_d are model parameters reflecting the effect of particle interlock. All of these parameters can be obtained by triaxial shear tests.

(4) Added parameter: p_R. It denotes the tensile strength caused by mask chips and can be obtained by triaxial shear tests.

In conclusion, the parameters G_0, K_0 (or ν), n, e_{ref}, λ, ζ can be obtained by isotropic compression tests. The parameters φ_c, k_p, A_d, n_p, n_d, and p_R can be determined by triaxial shear tests. It is worth noting that the parameters λ, ζ, n_p, n_d should be determined through curve fitting.

5.4.2 Effects of model parameters on model responses

In this section, we mainly examine the influence of the parameters p_R, k_p, and n_p on the stress–strain relationship and dilatancy of MSM through consolidation-drained triaxial shear tests. The initial void ratio is given as $e_0 = 0.8$, and the effective confining pressure is 100 kPa. Trial values of p_R, k_p, and n_p are used, while the other parameters are listed in Table **5.2**.

First, numerical consolidation-drained triaxial shear tests with different p_R values are conducted to evaluate the ability of this model to describe the strength and deformation characteristics of MSM. As shown in Fig. 5.3**,** compared with pure sand ($p_R = 0$), the MSM shows higher shear strength. Meanwhile, an increase in p_R will give rise to an increase in the critical strength of MSM, which is consistent with the experimental observations in Section 2 that the CSL of MSM moves upwards in the q–p plane with the increase of c. Furthermore, it is observed that the MSM has a smaller dilatancy response. This means that the mask chip may enhance the anti-deformation ability of soils. This set of simulations shows that the engineering performance of soils is significantly improved by reinforcing with mask chips, and such improvements can be well reproduced by the proposed model.

Fig. **5.4** illustrates that the parameter k_p mainly controls the initial stiffness of the proposed model. Generally, with the increase of k_p, the model shows smaller stiffness and smaller dilatancy at the onset of loading; however, both the deviatoric stress–axial strain and volumetric strain–axial strain curves become identical after a sufficiently large axial strain, which indicates that the parameter k_p does not influence the critical state. Note that the volumetric strains in Fig. 5.4(b) do not reach the same critical state due to insufficient axial strain. This set of simulations suggests we can change this parameter to control the difference in initial stiffness between the pure sand and the MSM.

Fig. 5.5 presents the evolution of deviatoric stress–axial strain and volumetric strain–axial strain curves with various n_p values. In the case of n_p greater than unity, the deviatoric stress–axial strain curve gradually transitions from strain-hardening to strain-softening. Moreover, with the increase of n_p, the proposed model shows more pronounced strain-softening and dilatative volumetric strain behaviors.

5.4.3 Model validation with experimental data

We proceed to validate the proposed model by comparing model predictions to experimental tests on pure sand and MSMs. The consolidation-drained triaxial shear test results in Section 2 are used, and the model parameters are calibrated by the experimental data, as shown in Table **5.3**.

Fig. 5.6 shows the comparison between the experimental and numerical tests on pure sand, MSM-I, MSM-II, and MSM-III under different effective confining pressures and initial densities. Clearly, the overall shear strength of MSM is significantly enhanced with the increase of the p_R value. In addition, the MSM exhibits a smaller initial stiffness attributed to the effect of mask chips when compared to pure sand. For instance, under the same initial density and effective confining pressure, the axial strain corresponding to the peak deviatoric stress of each MSM sample is consistently greater than that of pure sand. Furthermore, it can be observed that the proposed model effectively describes the stress–strain relationship and dilatancy characteristics of pure sand, as well as the stress–strain relationship of MSM with a higher initial density (D_r = 90%); however, it slightly overestimates the volumetric dilatancy of MSM with a relative density of D_r = 90%. For the MSM sample with a relative density of D_r = 60%, the model predictions align well with the experimental deviatoric stress–axial strain curves under lower stress levels, while the shear strength of MSM under higher stress levels, particularly when the effective confining pressure equals 200 kPa, is underestimated. Overall, the proposed model can well reproduce the evolution of initial stiffness, strength, and dilatancy of both pure sand and MSMs under various effective confining pressures and initial densities.

Since there are currently no available constitutive models for MSM, in what follows, therefore, we will compare our model with a constitutive model for fiber-reinforced sands proposed by Diambra et al. (2013). In their constitutive framework, the model is divided into two parts, one for sand matrix and is described by the Severn-Trent sand model and the other for flex fiber following a linear elastic relationship. The former requires 3 parameters, while the latter needs 10 parameters. The combined contribution of fiber and sand to the mechanical behavior of fiber-reinforced sand is evaluated by the volumetric homogenization procedure.

The comparison between model predictions and experimental results shows that both our model and Diambra's model can successfully reproduce the static features of flexible fiber-reinforced sands, including enhanced stress–strain relationship, stress level dependency, and lower compressibility. The advantage of Diambra's model over our model is the fiber orientation is considered, which leads to their model being able to describe anisotropic behaviors of fiber-reinforced sands. However, due to Diambra's model being built on the superposition of stress and strain states of fibers and sands, it cannot reflect the interface interaction between fibers and sands. Moreover, without consideration of the orientation of mask chips, our model has a simpler and more elegant formulation, which enables our model to be implemented into a finite element code more easily.

5.5 Summary

This paper presents a critical state constitutive model for a mask chips-granular soil mixture based on experimental observation. It is developed by incorporating a non-associated flow rule within the framework of elastoplastic. To properly capture the tensile strength induced by mask chips, a new parameter (p_R) is introduced into the yield function, plastic potential, and the elastic modulus. This enables our model to capture the variation of stiffness, strength, and deformation with mask chip contents and stress levels. The proposed model requires 12 parameters, and all of them can be conveniently calibrated based on the conventional laboratory test and curve fitting. The proposed model is further validated by a series of triaxial shear tests on both pure sands and mask chips reinforced sands under loading conditions with various effective confining pressures and initial densities. The results show that our model can properly describe the strength and deformation characteristics of the mask chips-granular soil mixture, including the initial stiffness, shear strength, and volumetric dilatancy.

The proposed model serves as a powerful tool for simulating mask chips reinforced sands in general stress states. It provides valuable insights for the practical application of mask chips reinforced soil in engineering. However, further improvements are pursued for future work. For instance, the model could be enhanced by considering the orientation of mask chips and the de-bonding process, which would offer a more comprehensive understanding of the mechanical behaviors of the mask chips-granular soil mixture.

Table 5.1Physical parameters of pure sand and MSMs

Materials	d_{50} (mm)	C_u	C_c	G_s	Sand Maximum dry density ρ_{dmax} (g/cm^3)	Minimum dry density ρ_{dmin} (g/cm^3)	Maximum void ratio e_{max}	Minimum void ratio e_{min}	Mask chips Content	Size (mm×mm)
Pure sand	0.70	1.30	0.84	2.64	1.67	1.40	0.882	0.582	0	0
MSM-I									0.5%	10×10
MSM-II									0.5%	12×3
MSM-III									0.5%	20×5

Table 5.2 Model parameters for numerical simulations

Elastic parameters	Critical state parameters	Plastic shear parameters	Parameter related to the reinforcement effect of mask chips on MSM
G_0=100 K_0=166.67 n=0.10	e_{ref}=0.937 λ_3=0.022 ζ_3=0.71 φ_c=30.00°	k_p=0.005 A_d=2.00 n_p=1.00 n_d=1.00	p_R=0

Table 5.3 Model parameters of pure sand and MSMs

Materials	G_0	K_0	n	e_{ref}	λ_3	ζ_3	φ_c	k_p	A_d	n_p	n_d	p_R
Pure sand	55	91.67	0.84	0.845	0.026	1.00	32.8	0.002	0.43	2.00	2.00	0.00
MSM-I								0.02		5.00		28.88
MSM-II								0.02		5.00		16.51
MSM-III								0.02		5.00		43.74

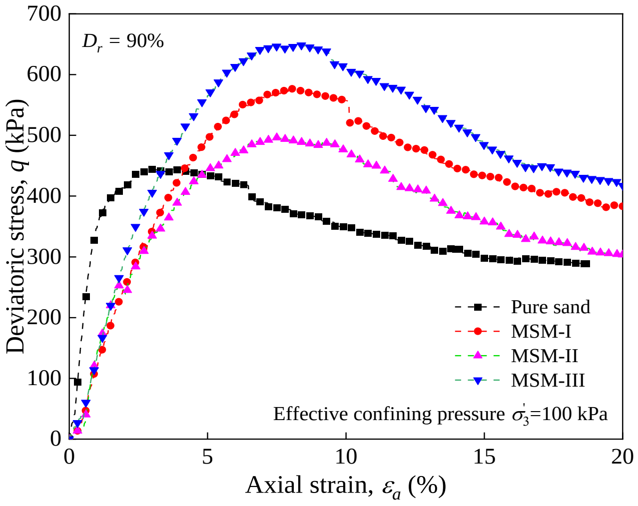

(a)

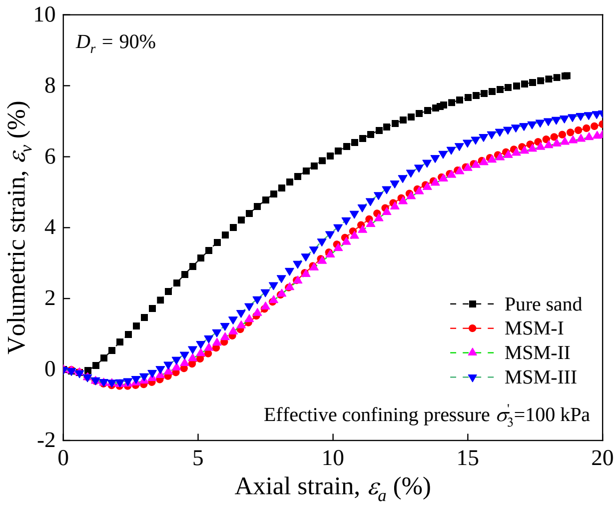

(b)

Fig. 5.1 Mechanical behaviors of pure sand and MSMs: (a) Deviatoric stress axial strain curves; (b) Volumetric strain axial strain curves

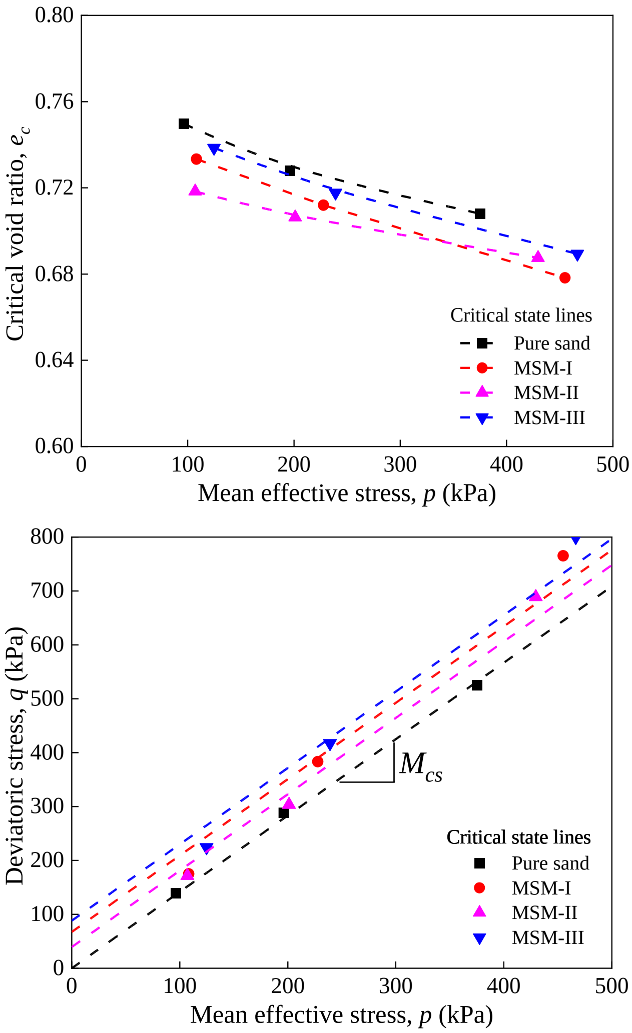

(a)

(b)

Fig. 5.2 Critical state lines for pure sand and MSMs: (a) in the e–p plane; and (b) in the q–p plane

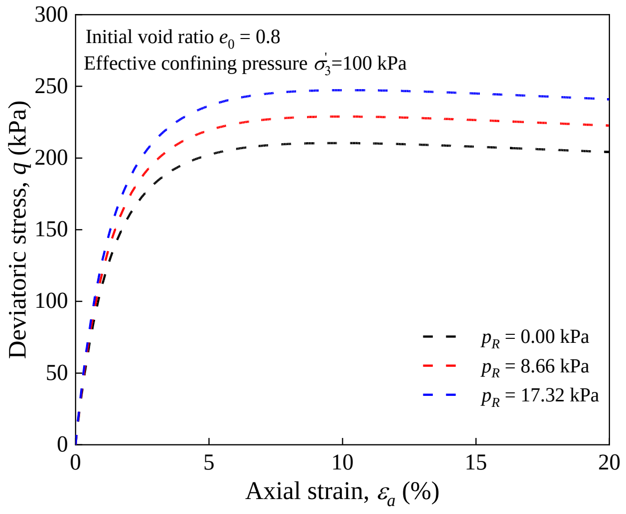

(a)

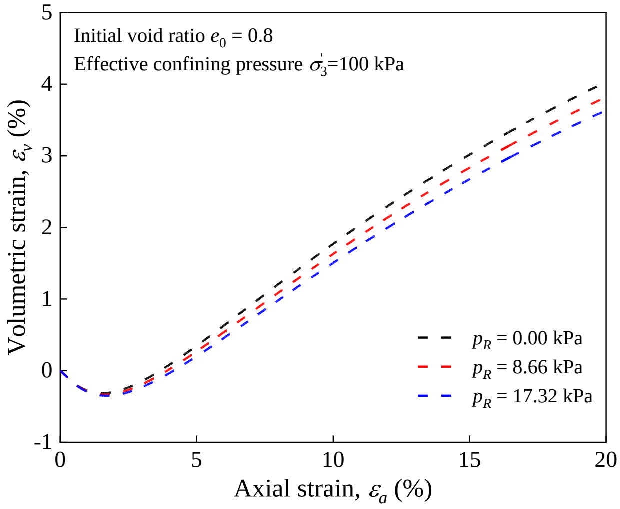

(b)

Fig. 5.3 The effects of parameter p_R on the model performance: (a) Deviatoric stress axial strain curves; (b) Volumetric strain axial strain curves

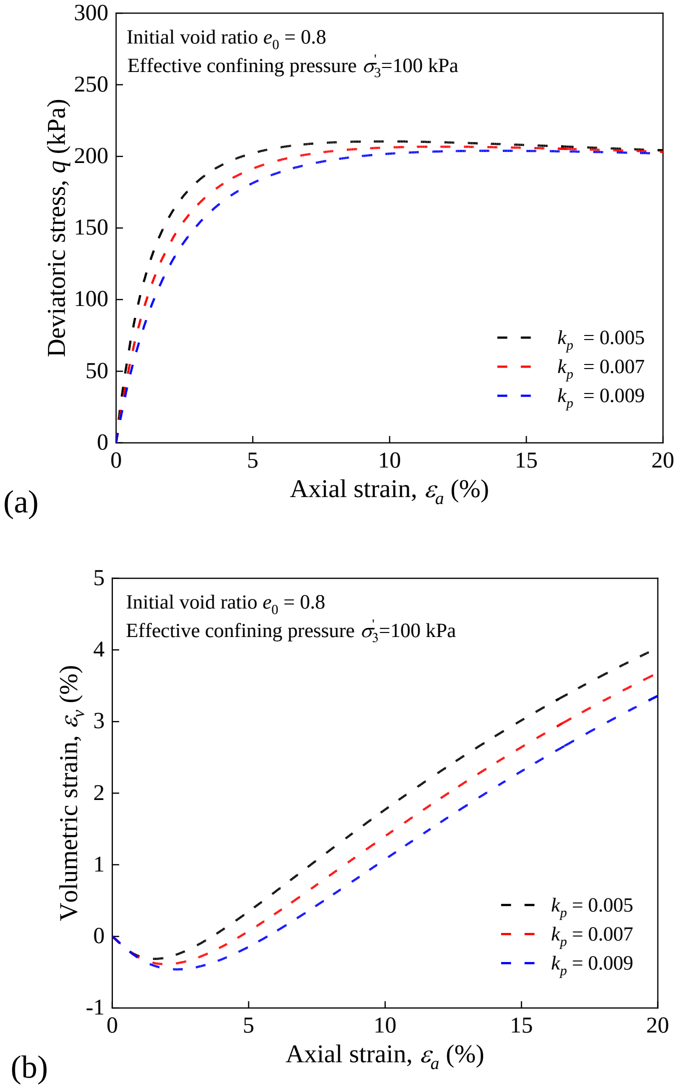

Fig. 5.4 The effects of parameter k_p on the model performance: (a) Deviatoric stress axial strain curves; (b) Volumetric strain axial strain curves

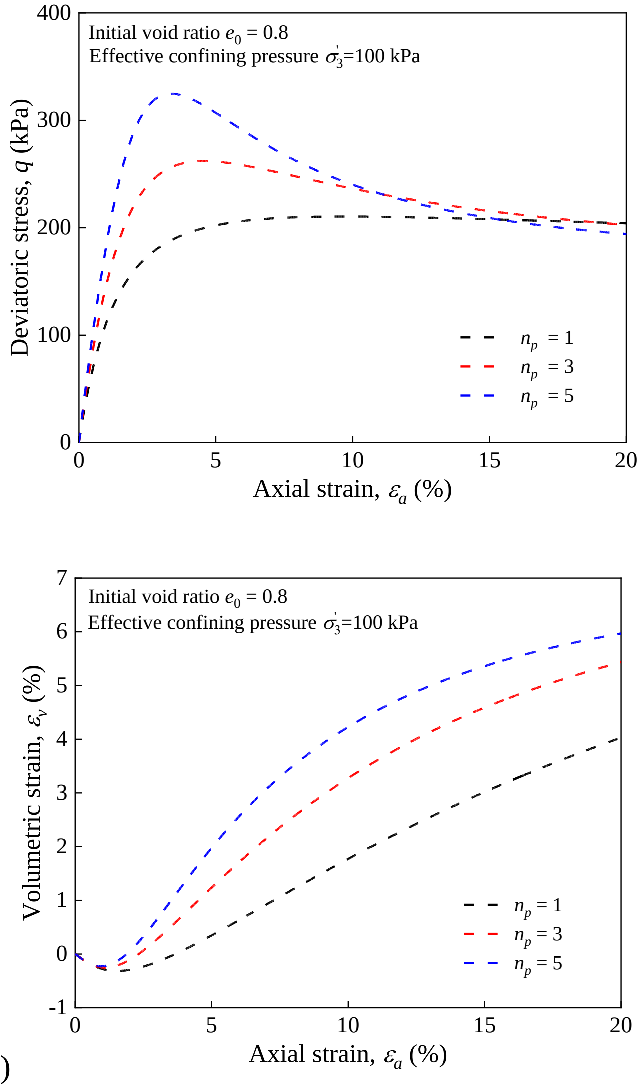

(a)

(b)

Fig. 5.5 The effects of parameter n_p on the model performance: (a) Deviatoric stress axial strain curves; (b) Volumetric strain axial strain curves

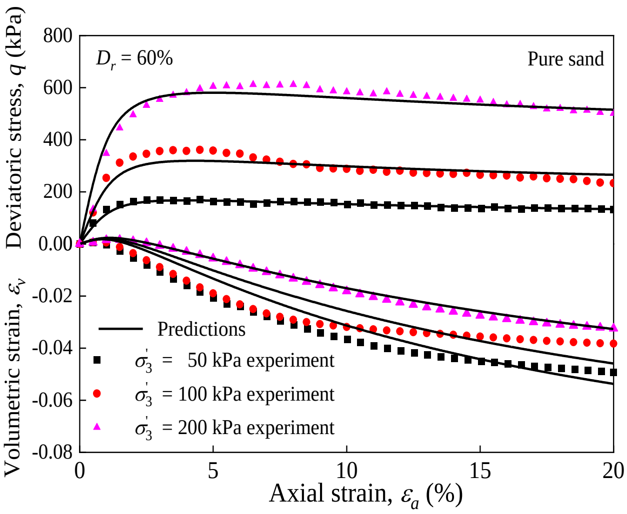

(a)

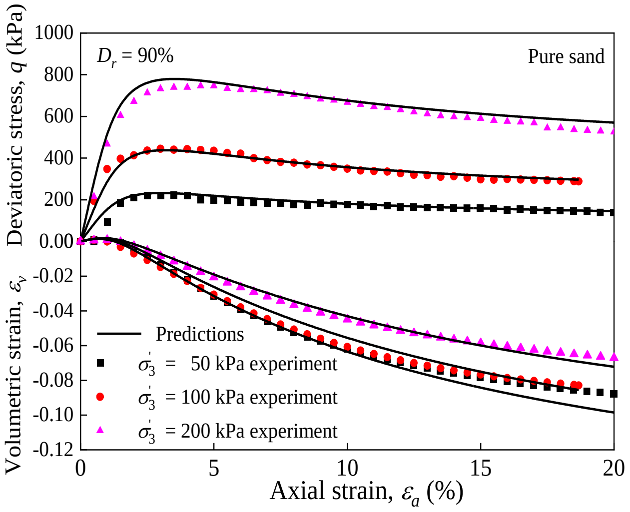
Deviatoric stress, q (kPa)
Volumetric strain, ε_v
1000
800
600
400
200
0.00
-0.02
-0.04
-0.06
-0.08
-0.10
-0.12
D_r = 90%
Pure sand
Predictions
σ_3' = 50 kPa experiment
σ_3' = 100 kPa experiment
σ_3' = 200 kPa experiment
0
5
10
15
20
Axial strain, ε_a (%)

(b)

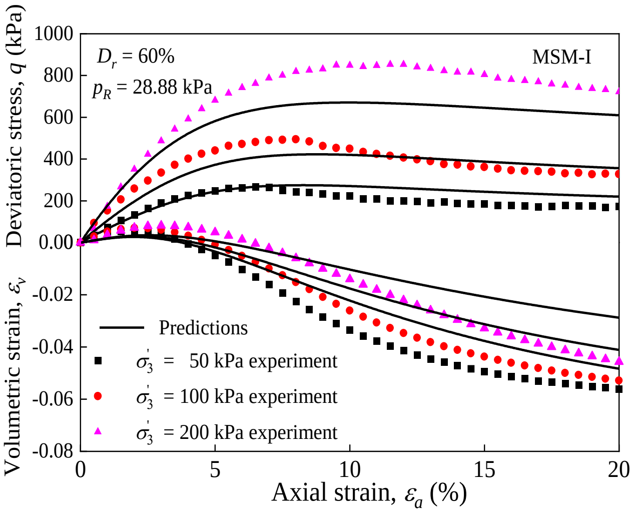
Deviatoric stress, q (kPa)
Volumetric strain, ε_v
1000
800
600
400
200
0.00
-0.02
-0.04
-0.06
-0.08
D_r = 60%
p_R = 28.88 kPa
MSM-I
Predictions
σ_3' = 50 kPa experiment
σ_3' = 100 kPa experiment
σ_3' = 200 kPa experiment
0
5
10
15
20
Axial strain, ε_a (%)

(c)

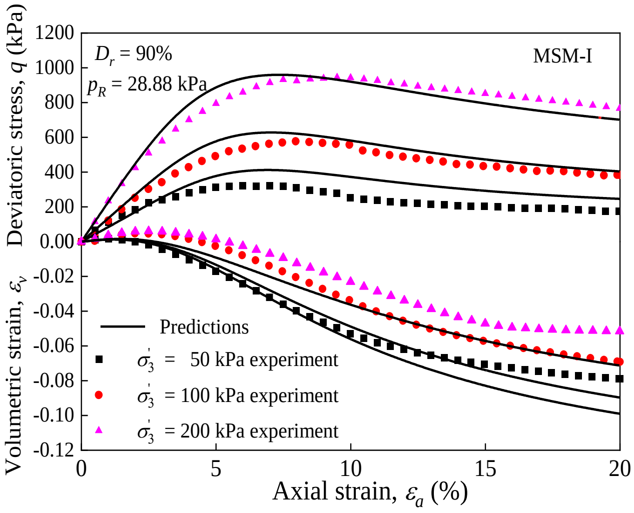
Deviatoric stress, q (kPa)
Volumetric strain, ε_v
1200
1000
800
600
400
200
0.00
-0.02
-0.04
-0.06
-0.08
-0.10
-0.12
D_r = 90%
p_R = 28.88 kPa
MSM-I
Predictions
σ_3' = 50 kPa experiment
σ_3' = 100 kPa experiment
σ_3' = 200 kPa experiment
0
5
10
15
20
Axial strain, ε_a (%)

(d)

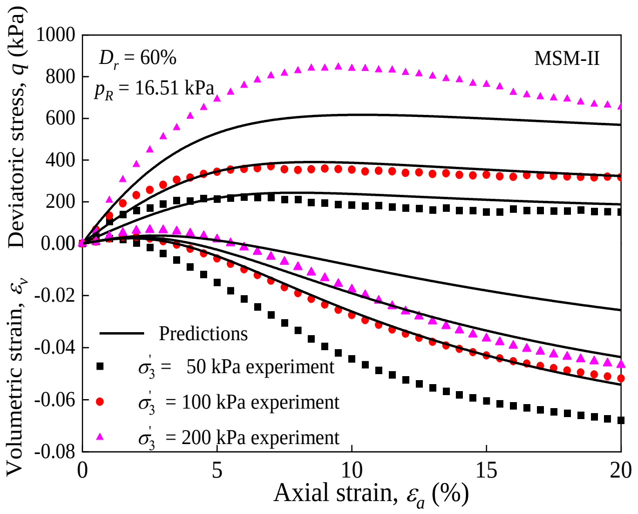
D_r = 60%
p_R = 16.51 kPa
MSM-II
Deviatoric stress, q (kPa)
Volumetric strain, ε_v
1000
800
600
400
200
0.00
-0.02
-0.04
-0.06
-0.08
Predictions
σ_3' = 50 kPa experiment
σ_3' = 100 kPa experiment
σ_3' = 200 kPa experiment
0
5
10
15
20
Axial strain, ε_a (%)

(e)

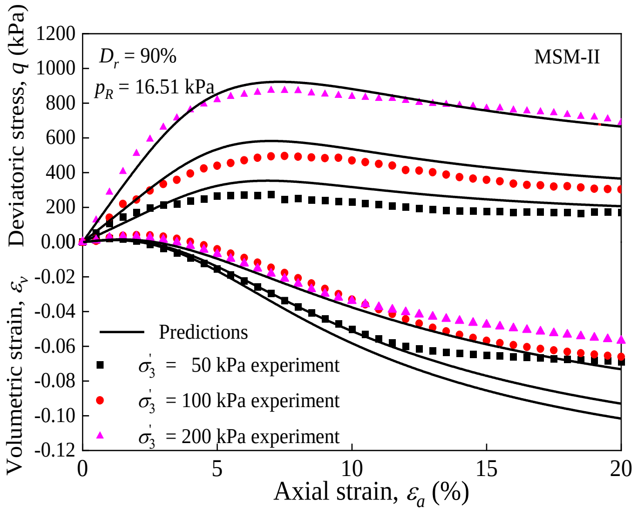
D_r = 90%
p_R = 16.51 kPa
MSM-II
Deviatoric stress, q (kPa)
Volumetric strain, ε_v
1200
1000
800
600
400
200
0.00
-0.02
-0.04
-0.06
-0.08
-0.10
-0.12
Predictions
σ_3' = 50 kPa experiment
σ_3' = 100 kPa experiment
σ_3' = 200 kPa experiment
0
5
10
15
20
Axial strain, ε_a (%)

(f)

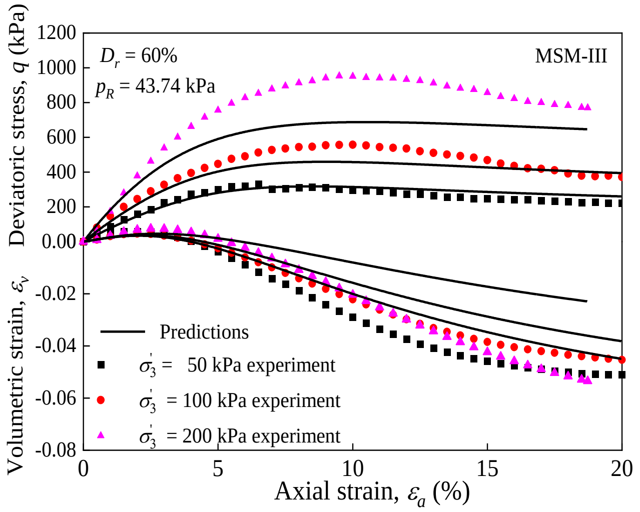
D_r = 60%
p_R = 43.74 kPa
MSM-III
Deviatoric stress, q (kPa)
Volumetric strain, ε_v
1200
1000
800
600
400
200
0.00
-0.02
-0.04
-0.06
-0.08
Predictions
σ_3' = 50 kPa experiment
σ_3' = 100 kPa experiment
σ_3' = 200 kPa experiment
0
5
10
15
20
Axial strain, ε_a (%)

(g)

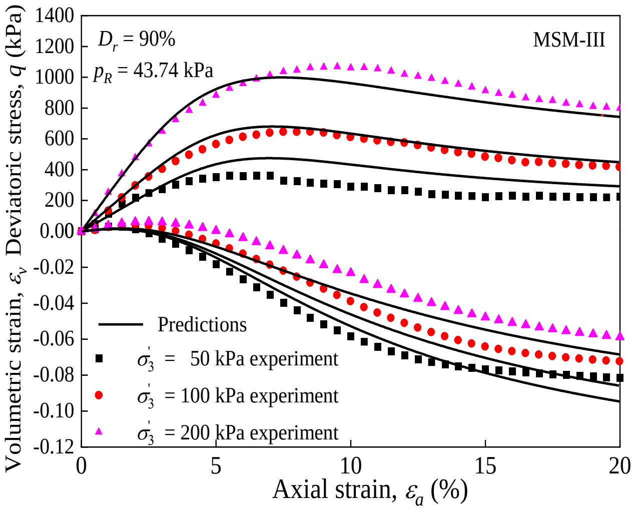

(h)

Fig. 5.6 Comparison between numerical and experimental consolidation-drained triaxial shear tests on pure sand and MSMs: (a, b) pure sand; (c, d) MSM-I ; (e, f) MSM-II; (g, h) MSM-III

Chapter 6 Conclusions and Future Work

6.1 General summary

In practical projects discrete granular material is commonly used as filling material in the construction of roadbeds. During the use of the roadbed the discrete granular material suffers from extensive cyclic dynamic loads, causing sand loss or shear failures which results in the road surface settlement and collapse. The existing studies have investigated the function of additives such as rubber, geotextile, cement, polynomial fiber on the sand strength improvement. However, either the performance is not as the expectation or the chemical in the additive will harm environment. Since the outbreak of COVID-19 the emergence of a large amount of discarded masks has made their disposal a serious problem. Mask chips are flexible material with certain tensile strength, therefore in recent years sterilized mask chips have become popular as an additive to enhance the strength of granular material, which can not only reduce the harm to ecosystem but also can save the energy. The optimal content of the mask chips and the micro mechanisms of strength enhancement under isotropic static loading and dynamic loading have been widely investigated. Except the granular materials many researchers have investigated the effect of weight fraction, length of mask chips and initial effective pressure on mechanical properties of materials such as complete decomposed granite, clay, recycled concrete aggregate and hot asphalt etc. under monotonic triaxial stress condition and cyclic dynamic stress condition. However, the shape designed for mask cutting which will guide the application of discarded mask usage in real engineering project has not been investigated, thereby this work studies the best surface area and aspect ratio of mask chips under two different static stress states. The cyclic dynamic stress route will be investigated in future work due to the limitation of the study period. The current constitutive model cannot well predict the mechanical behavior of the discrete granular material reinforced with mask chips due to the additive, mask chips, could provide extra tensile strength and wrapping strength to discrete granular material to enhance its mechanical property. Therefore, in this thesis a state dependent elastoplastic constitutive model referred to Yin’s SIMSAND model is proposed to describe the mechanical characteristics of MSM. The predictive ability of this new constitutive model is validated by the triaxial experiment results.

6.1.1 Strength and Deformation Properties of Enhanced Granular Material

At relative higher sample internal stress condition, the relative density and confining pressure play an important role on the stiffness because more particles provide the supporting force to resist the deformation. The peak compression resistance of high-density granular material is higher than that of medium density pure granular material because more particles provide skeletal force, locking force and frictional force (both static frictional angle and dynamic frictional angle play a role in compression resistance), while the residual compression resistance of the high-density granular material is almost the same as that of the medium density granular materials because only the dynamic frictional force were left and the dynamic frictional force provide by the particles on the failure surface have little difference for high-density granular material and medium dense granular material.

The relative density has a great influence on the compression and dilatancy processes. The compression behavior for the sand with lower relative density is more obvious and last longer because more pore that allow sand particles fill in exist between loose granular particles, while the dilatancy happens earlier and more obvious for dense sand than that of loose sand since the dense particles are more prone to mismove, roll, lift and pull out, resulting in an increase of the pore volume between soil particles.

Besides, the confining pressure also affects the sample deformation, which means the higher the relative confining pressure the more obvious the compression process and the less obvious the dilatation process. From a microscope point of view to explain this phenomenon is that during the loading period the restriction resulting from medium and minimum confining pressure on the horizontal displacement of the sand particles cause the sample particles to move downwards to fill the voids instead of a particle rolling or a particle lift which generates the void, therefore, intensify the compression process and suppress the dilatancy process.

6.1.2 Experimental study under biaxial shear condition

The study concluded that the inclusion of mask chips enhances the strength and delays the stress peak, with 20 mm × 5 mm chips showing the best reinforcement performance. The strain corresponding to the peak stress also increased with the presence of mask chips. The mask-chips-reinforced sand underwent greater compression during the contraction stage, which could be due to changes in particle arrangement and packing. Two distinct shear band shapes were observed, with the mask chips playing an insignificant role in their formation. The dimensionless parameter η correlated the mask chip size and mean diameter of the grain particles, indicating a positive correlation between strength improvement and this parameter.

These findings contribute to a better understanding of the mechanical behavior of sand reinforced with mask chips, offering potential applications in ground improvement and geotechnical engineering. Additionally, it addresses the important matter of recycling and reusing disposable masks.

6.1.3 Elastoplastic constitutive model

This part presents a critical state constitutive model for a mask chips-granular soil mixture based on experimental observation. It is developed by incorporating a non-associated flow rule within the framework of elastoplastic. To properly capture the tensile strength induced by mask chips, a new parameter (p_R) is introduced into the yield function, plastic potential, and the elastic modulus. This enables our model to capture the variation of stiffness, strength, and deformation with mask chip contents and stress levels. The proposed model requires 12 parameters, and all of them can be conveniently calibrated based on the conventional laboratory test and curve fitting. The proposed model is further validated by a series of triaxial shear tests on both pure sands and mask chips reinforced sands under loading conditions with various effective confining pressures and initial densities. The results show that our model can properly describe the strength and deformation characteristics of the mask chips-granular soil mixture, including the initial stiffness, shear strength, and volumetric dilatancy.

6.2 Recommendations for Future Research

Based on the work of this thesis, the author recognizes that research in some areas still needs to be conducted in future as follows.

Future research could focus on various relative densities of the sand, cyclic loadings, and long-term performance to further optimize the reinforcement properties. However, the need to customize mask dimensions introduces additional processing costs, adding an economic aspect to the methodology. Therefore, careful consideration and balance of these factors are crucial for the successful implementation of this approach.

The proposed elastoplastic constitutive model serves as a powerful tool for simulating mask chips reinforced sands in general stress states. It provides valuable insights for the practical application of mask chips reinforced soil in engineering. However, further improvements are pursued for future work. For instance, the model could be enhanced by considering the orientation of mask chips and the de-bonding process, which would offer a more comprehensive understanding of the mechanical behaviors of the mask chips-granular soil mixture.

References

Akarsu, C., et al. (2021). "Characterization of littered face masks in the southeastern part of Turkey." Environmental Science and Pollution Research **28**(34): 47517-47527.

Akhbarizadeh, R., et al. (2021). "Abandoned Covid-19 personal protective equipment along the Bushehr shores, the Persian Gulf: an emerging source of secondary microplastics in coastlines." Marine pollution bulletin **168**: 112386.

Aragaw, T. A. (2020). "Surgical face masks as a potential source for microplastic pollution in the COVID-19 scenario." Marine pollution bulletin **159**: 111517.

Benson, N. U., et al. (2021). "COVID pollution: impact of COVID-19 pandemic on global plastic waste footprint." Heliyon **7**(2).

Betsch, C., et al. (2020). "Social and behavioral consequences of mask policies during the COVID-19 pandemic." Proceedings of the National Academy of Sciences **117**(36): 21851-21853.

Bondaroff, T. P., et al. (2020). "Masks on the beach." The impact of Covid-19 on Marine Plastic Pollution.

Chowdhury, T., et al. (2022). "Estimation of the healthcare waste generation during COVID-19 pandemic in Bangladesh." Science of the Total Environment **811**: 152295.

Ciotti, M., et al. (2020). "The COVID-19 pandemic." Critical reviews in clinical laboratory sciences **57**(6): 365-388.

Dharmaraj, S., et al. (2021). "The COVID-19 pandemic face mask waste: a blooming threat to the marine environment." Chemosphere **272**: 129601.

Haleem, A., et al. (2020). "Effects of COVID-19 pandemic in daily life." Current medicine research and practice **10**(2): 78.

Li, T., et al. (2020). "Mask or no mask for COVID-19: A public health and market study." Plos one **15**(8): e0237691.

Luhar, I., et al. (2022). "Challenges and impacts of COVID-19 pandemic on global waste management systems: A Review." Journal of Composites Science **6**(9): 271.

Mejjad, N., et al. (2021). "Disposal behavior of used masks during the covid-19 pandemic in the Moroccan community: potential environmental impact." International journal of environmental research and public health **18**(8): 4382.

Mobarak, M. B., et al. (2022). "Covid-19 waste facemask conundrum: A facile way of utilization through fabricating composite material with unsaturated polyester resin and evaluation of its mechanical properties." Heliyon **8**(12).

Pourebrahimi, S. (2022). "Upcycling face mask wastes generated during COVID-19 into value-added engineering materials: A review." Science of the Total Environment **851**: 158396.

Rajkhowa, S. and J. Sarma (2023). "Biomedical Waste During COVID-19: Status, Management, and Treatment." One Health: Human, Animal, and Environment Triad: 161-168.

Rakib, M. R. J., et al. (2021). "Personal protective equipment (PPE) pollution driven by the COVID-19 pandemic in Cox's Bazar, the longest natural beach in the world." Marine pollution bulletin **169**: 112497.

Sangkham, S. (2020). "Face mask and medical waste disposal during the novel COVID-19 pandemic in Asia." Case Studies in Chemical and Environmental Engineering **2**: 100052.

Scheid, J. L., et al. (2020). "Commentary: physiological and psychological impact of face mask usage during the COVID-19 pandemic." International journal of environmental research and public health **17**(18): 6655.

Shetty, S. S., et al. (2020). "Discarded Covid 19 gear: A looming threat." Oral Oncology **107**: 104868.

Shruti, V., et al. (2020). "Reusable masks for COVID-19: a missing piece of the microplastic problem during the global health crisis." Marine pollution bulletin **161**: 111777.

Tan, M., et al. (2021). "How the public used face masks in China during the coronavirus disease pandemic: A survey study." International journal of nursing studies **115**: 103853.

Tesfaldet, Y. T. and N. T. Ndeh (2022). "Assessing face masks in the environment by means of the DPSIR framework." Science of the Total Environment **814**: 152859.

Tirupathi, R., et al. (2020). "Comprehensive review of mask utility and challenges during the COVID-19 pandemic." Infez Med **28**(suppl 1): 57-63.

Kaewchutima N, Precha N, Duangkong N, et al. Knowledge and practice of facemask disposal among university students in Thailand: A new normal post the COVID-19 pandemic[J]. Plos one, 2023, 18(4): e0284492

Jayasinghe R R, Abeyrathna W P, Lythgoe D, et al. Analysis of the community behavioural patterns in management of household plastic waste due to the COVID-19 pandemic in

Sri Lanka[J]. Case Studies in Chemical and Environmental Engineering, 2022, 6: 100246

Shammi M, Tareq S M. Environmental catastrophe of COVID-19: disposal and management of PPE in Bangladesh[J]. Global Social Welfare, 2021, 8: 133-136

Sangkham S. Face mask and medical waste disposal during the novel COVID-19 pandemic in Asia[J]. Case Studies in Chemical and Environmental Engineering, 2020, 2: 100052

Sharma H B, Vanapalli K R, Cheela V R S, et al. Challenges, opportunities, and innovations for effective solid waste management during and post COVID-19 pandemic[J]. Resources, conservation and recycling, 2020, 162: 105052

Yang W, Cao L, Li W, et al. Carbon Nanotube prepared by catalytic pyrolysis as the electrode for supercapacitors from polypropylene wasted face masks[J]. Ionics, 2022, 28(7): 3489-3500

Peng Y, Wang Y, Ke L, et al. A review on catalytic pyrolysis of plastic wastes to high-value products[J]. Energy Conversion and Management, 2022, 254: 115243

Cui J, Qi M, Zhang Z, et al. Disposal and resource utilization of waste masks: a review[J]. Environmental Science and Pollution Research, 2023, 30(8): 19683-19704.

Ilyas S, Srivastava R R, Kim H. Disinfection technology and strategies for COVID-19 hospital and bio-medical waste management[J]. Science of the Total Environment, 2020, 749: 141652

Idrees M, Akbar A, Mohamed A M, et al. Recycling of waste facial masks as a construction material, a step towards sustainability[J]. Materials, 2022, 15(5): 1810

Selvaranjan K, Navaratnam S, Rajeev P, et al. Environmental challenges induced by extensive use of face masks during COVID-19: A review and potential solutions[J]. Environmental Challenges, 2021, 3: 100039

Ahmed W, Lim C W. Effective recycling of disposable medical face masks for sustainable green concrete via a new fiber hybridization technique[J]. Construction and Building Materials, 2022, 344: 128245

Avudaiappan S, Cendoya P, Arunachalam K P, et al. Innovative Use of Single-Use Face Mask Fibers for the Production of a Sustainable Cement Mortar[J]. Journal of Composites Science, 2023, 7(6): 214

Zhang J Q, Wang X, Yin Z Y, et al. Static and dynamic behaviors of granular soil reinforced by disposable face-mask chips[J]. Journal of Cleaner Production, 2022, 331: 129838

Xu W, Yin Z Y, Wang H L, et al. Experimental study on the monotonic mechanical behavior of completely decomposed granite soil reinforced by disposable face-mask chips[J]. Journal of Cleaner Production, 2022, 352: 131528

Idrees M, Akbar A, Mohamed A M, et al. Recycling of waste facial masks as a construction material, a step towards sustainability[J]. Materials, 2022, 15(5): 1810

Avudaiappan S, Cendoya P, Arunachalam K P, et al. Innovative Use of Single-Use Face Mask Fibers for the Production of a Sustainable Cement Mortar[J]. Journal of Composites Science, 2023, 7(6): 214

Parija S, Mishra D, Leung C. Preliminary Results of Concrete with Shredded Disposable Face Masks[C]//Proceedings of the 35th Indian Engineering Congress (IEC)—Engineering for Self Reliance and Sutainable Goals, Kolkata, India. 2020: 18-20

Ghadr S, Chen C S, Liu C, et al. Mechanical behavior of sands reinforced with shredded face masks[J]. Bulletin of Engineering Geology and the Environment, 2022, 81(8): 317

Said S, Rahhal M E. Improving the compaction properties and shear resistance of a sand reinforced with COVID-19 waste mask fibers[J]. Heliyon, 2022, 8(12)

Zhang J Q, Wang X, Yin Z Y, et al. Static and dynamic behaviors of granular soil reinforced by disposable face-mask chips[J]. Journal of Cleaner Production, 2022, 331: 129838）

Alshibli Khalid, A., and Sture, S. (2000). "Shear Band Formation in Plane Strain Experiments of Sand." *J. Geotech. Geoenviron. Eng.*, 126(6), 495-503.

Amy, P., Yi, C., Lei, L., Wang, X., Xuanze, Y., Haotian, W., Mervin, Z., Qiqi, W., Steven, C., and Larry, C. (2020). "Is the fit of N95 facial masks effected by disinfection? A study of heat and UV disinfection methods using the OSHA protocol fit test." *medRxiv*, 2020.2004.2014.20062810.

Arthur, J. R. F., Dunstan, T., Al-Ani, Q. A. J. L., and Assadi, A. (1977). "Plastic deformation and failure in granular media." *Géotechnique*, 27(1), 53-74.

Asim, N., Badiei, M., and Sopian, K. (2021). "Review of the valorization options for the proper disposal of face masks during the COVID-19 pandemic." *Environ. Technol. Innovation*, 23, 101797.

Dos Santos, A. P. S., Consoli, N. C., and Baudet, B. A. (2010). "The mechanics of fibre-reinforced sand." *Géotechnique,* 60(10), 791-799.

Ganiev, J., Yamada, S., Nakano, M., and Sakai, T. (2022). "Effect of fiber-reinforcement on the mechanical behavior of sand approaching the critical state." *J. Rock Mech. Geotech. Eng.*, 14(4), 1241-1252.

Gu, X., Huang, M., and Qian, J. (2014). "Discrete element modeling of shear band in granular materials." *Theor. Appl. Fract. Mech.*, 72, 37-49.

Gui, Y., Wong Weng, Y., and Gallage, C. (2022). "Effectiveness and Sensitivity of Fiber Inclusion on Desiccation Cracking Behavior of Reinforced Clayey Soil." *Int. J. Geomech.*, 22(3), 06021040.

Han, C., and Drescher, A. (1993). "Shear Bands in Biaxial Tests on Dry Coarse Sand." *Soils Found.*, 33(1), 118-132.

Hassoun, M., Villard, P., Al Heib, M., and Emeriault, F. (2018). "Soil Reinforcement with Geosynthetic for Localized Subsidence Problems: Experimental and Analytical Analysis." *Int. J. Geomech.*, 18(10), 04018133.

Hossini, H., Atashkar, S., and Massahi, T. (2021). "Face Mask Consumption and Medical Waste Generation During the COVID-19 Pandemic in Iran: Challenges and Problems." *J Health Rep Technol*, 7(3), e115046.

Karaivanov, A., Lu, S. E., Shigeoka, H., Chen, C., and Pamplona, S. (2021). "Face masks, public policies and slowing the spread of COVID-19: Evidence from Canada." *Journal of Health Economics*, 78(102475).

Khodabandehlou, S., Makarchian, M., and Razmara, M. (2023). "Effect of polypropylene fibre reinforcement on UCS and ductility of cemented sand." *Proceedings of the Institution of Civil Engineers - Geotechnical Engineering*, 176(1), 42-48.

Kuhn, M. R. (2017). "4 - Loading, Movement, and Strength." *Granular Geomechanics*, M. R. Kuhn, ed., Elsevier, 153-227.

Li, L., Zang, T., Xiao, H., Feng, W., and Liu, Y. (2020). "Experimental study of polypropylene fibre-reinforced clay soil mixed with municipal solid waste incineration bottom ash." *Eur. J. Environ. Civ. Eng.*, 1-17.

Lunag, M. N., Abana, A. S., Agcaoili, J. P., Arellano, J. K. T., Caluza, C. A. G., Decena, N. B. V., Paz, E. R. D., Delgado, L. A. B., Obero, A. F., Ocampo, D. M. E., and Sacdalan, C. A. D. (2023). "Face mask and medical waste generation in the City of Baguio, Philippines: its current management and GHG footprint." *J. Mater. Cycles Waste Manage.*, 25(2), 1216-1226.

Lv, C., Zhu, C., Tang, C. S., Cheng, Q., Yin, L. Y., and Shi, B. (2021). "Effect of fiber reinforcement on the mechanical behavior of bio-cemented sand." *Geosynth Int*, 28(2), 195-205.

Madhusudhan, B. N., Baudet, B. A., Ferreira, P. M. V., and Sammonds, P. (2017). "Performance of Fiber Reinforcement in Completely Decomposed Granite." *J. Geotech. Geoenviron. Eng.*, 143(8), 04017038.

Maheshwari, B. K., Singh, H. P., and Saran, S. (2012). "Effects of Reinforcement on Liquefaction Resistance of Solani Sand." *J. Geotech. Geoenviron. Eng.*, 138(7), 831-840.

Miranda Pino, L. F., and Baudet, B. A. (2015). "The effect of the particle size distribution on the mechanics of fibre-reinforced sands under one-dimensional compression." *Geotext. Geomembr.*, 43(3), 250-258.

Mirzaalimohammadi, A., Ghazavi, M., Lajevardi, S. H., and Roustaei, M. (2021). "Experimental Investigation on Pullout Behavior of Geosynthetics with Varying Dimension." *Int. J. Geomech.*, 21(6), 04021089.

Muir Wood, D., Diambra, A., and Ibraim, E. (2016). "Fibres and soils: A route towards modelling of root-soil systems." *Soils Found.*, 56(5), 765-778.

Nzediegwu, C., and Chang, S. X. (2020). "Improper solid waste management increases potential for COVID-19 spread in developing countries." *Resour Conserv Recycl*, 161(104947).

Palmeira, E. M., and Góngora, I. A. G. (2015). "Assessing the Influence of Some Soil–Reinforcement Interaction Parameters on the Performance of a Low Fill on Compressible Subgrade. Part I: Fill Performance and Relevance of Interaction Parameters." *International Journal of Geosynthetics and Ground Engineering*, 2(1), 1.

Priyadarshee, A., Chotu, A. K., and Kumar, V. (2014). "Effect of Fiber Properties on the strength of Fiber Reinforced Soil: A Review." *International Conference on Advances In Engineering And Technology - ICAET 2014*RIT, Roorkee, India.

Rattez, H., Shi, Y., Sac-Morane, A., Klaeyle, T., Mielniczuk, B., and Veveakis, M. (2022). "Effect of grain size distribution on the shear band thickness evolution in sand." *Géotechnique*, 72(4), 350-363.

Roscoe, K. H. (1970). "The influence of strains in soil mechanics." *Géotechnique*, 20, 129-170.

Saberian, M., Li, J., Kilmartin-Lynch, S., and Boroujeni, M. (2021). "Repurposing of COVID-19 single-use face masks for pavements base/subbase." *Sci Total Environ*, 769, 145527.

Sadek, S., Najjar, S. S., and Freiha, F. (2010). "Shear Strength of Fiber-Reinforced Sands." *J. Geotech. Geoenviron. Eng.*, 136(3), 490-499.

Silveira, M. R., Rocha, S. A., Correia, N. D., Rodrigues, R. A., Giacheti, H. L., and Lodi, P. C. (2021). "Effect of Polypropylene Fibers on the Shear Strength–Dilation Behavior of Compacted Lateritic Soils." *Sustainability*, 12603.

Sujatha, E. R., Atchaya, P., Darshan, S., and Subhashini, S. (2021). "Mechanical properties of glass fibre reinforced soil and its application as subgrade reinforcement." *Road Mater. Pavement Des.*, 22(10), 2384-2395.

Tang, C.-S., Li, H., Pan, X.-H., Yin, L.-Y., Cheng, L., Cheng, Q., Liu, B., and Shi, B. (2022). "Coupling effect of biocementation-fiber reinforcement on mechanical behavior of calcareous sand for ocean engineering." *Bull. Eng. Geol. Environ.*, 81(4), 163.

Vaverková, M. D., Paleologos, E. K., Dominijanni, A., Koda, E., Tang, C.-S., Małgorzata, W., Li, Q., Guarena, N., Mohamed, A.-M. O., Vieira, C. S., Manassero, M., O'Kelly, B. C., Xie, Q., Bo, M. W., Adamcová, D., Podlasek, A., Anand, U. M., Mohammad, A., Goli, V. S. N. S., Kuntikana, G., Palmeira, E. M., Pathak, S., and Singh, D. N. (2021). "Municipal solid waste management under Covid-19: challenges and recommendations." *Environ. Geotech.*, 8(3), 217-232.

Wang, K., and Brennan, A. (2019). "Behaviour of saturated fibre-reinforced sand in centrifuge model tests." *Soil Dyn. Earthquake Eng.*, 125, 105749.

Wang, P., Yin, Z.-Y., and Wang, Z.-Y. (2022). "Micromechanical Investigation of Particle-Size Effect of Granular Materials in Biaxial Test with the Role of Particle Breakage." *J. Eng. Mech.*, 148(1), 04021133.

Wang, W., and Chouw, N. (2017). "The behaviour of coconut fibre reinforced concrete (CFRC) under impact loading." *Constr. Build. Mater.*, 134, 452-461.

Wang, Y.-X., Guo, P.-P., Ren, W.-X., Yuan, B.-X., Yuan, H.-P., Zhao, Y.-L., Shan, S.-B., and Cao, P. (2017). "Laboratory Investigation on Strength Characteristics of Expansive Soil Treated with Jute Fiber Reinforcement." *Int. J. Geomech.*, 17(11), 04017101.

Wu, K., Liu, S., Sun, W., and Rémond, S. (2020). "DEM study of the shear behavior and formation of shear band in biaxial test." *Adv. Powder Technol.*, 31(4), 1431-1440.

Wu, K., Pizette, P., Becquart, F., Rémond, S., Abriak, N., Xu, W., and Liu, S. (2017). "Experimental and numerical study of cylindrical triaxial test on mono-sized glass beads under quasi-static loading condition." *Adv. Powder Technol.*, 28(1), 155-166.

Xu, D.-s., and Yin, J.-h. (2016). "Analysis of excavation induced stress distributions of GFRP anchors in a soil slope using distributed fiber optic sensors." *Eng. Geol.*, 213, 55-63.

Xu, W., Yin, Z.-Y., Wang, H.-L., and Wang, X. (2022). "Experimental study on the monotonic mechanical behavior of completely decomposed granite soil reinforced by disposable face-mask chips." *J. Cleaner Prod.*, 352, 131528.

Zhang, J.-Q., Wang, X., Yin, Z.-Y., and Yang, N. (2022). "Static and dynamic behaviors of granular soil reinforced by disposable face-mask chips." *J. Cleaner Prod.*, 331, 129838.

Zhao, F., and Zheng, Y. (2022). "Shear Strength Behavior of Fiber-Reinforced Soil: Experimental Investigation and Prediction Model." *Int. J. Geomech.*, 22(9), 04022146.

Anagnostopoulos, C.A., Tzetzis, D., Berketis, K. (2014). Evaluation of the shear strength behaviour of polypropylene and carbon fibre reinforced cohesive soils. *Research Journal of Applied Sciences, Engineering and Technology*, 7(20): 4327-4342. https://doi.org/10.19026/rjaset.7.805.

Biarez, J., Hicher, P.Y. (1994). Elementary mechanics of soil behaviors. Rotterdam: A.A. Balkema.

Dhawan, R., Bisht, B.M.S., Kumar, R., Kumari, S., Dhawan, S.K. (2019). Recycling of plastic waste into tiles with reduced flammability and improved tensile strength. *Process Safety and Environmental Protection*, 124: 299-307. https://doi.org/10.1016/j.psep.2019.02.018.

Diambra, A., Ibraim, E., Russell, A. R., Muir Wood, D. (2013). Fibre reinforced sands: from experiments to modelling and beyond. *International Journal for Numerical and Analytical Methods in Geomechanics*, 37(15): 2427-2455. https://doi.org/10.1002/nag.2142.

Fadare, O.O., Okoffo, E.D. (2020). Covid-19 face masks: A potential source of microplastic fibers in the environment. *The Science of the total environment*, 737: 140279. https://doi.org/10.1016/j.scitotenv.2020.140279.

Fathali, M., Nejad, F.M., Esmaeili, M. (2017). Influence of tire-derived aggregates on the properties of railway ballast material. *Journal of materials in civil engineering*, 29(1): 04016177. https://doi.org/10.1061/(asce)mt.1943-5533.0001702.

Gao Z, Lu D, Huang M. (2020). Effective skeleton stress and void ratio for constitutive modeling of fiber-reinforced sand. Acta geotechnica, 2020, 15: 2797-2811. https://doi.org/10.1007/s11440-020-00986-w.

Ghadr, S., Chen, C.S., Liu, C.h., Huang, C. (2022). Mechanical behavior of sands reinforced with shredded face masks. *Bulletin of Engineering Geology and the Environment*, 81: 317. https://doi.org/10.1007/s10064-022-02810-z.

Gudehus, G. (1997). Attractors, percolation thresholds and phase limits of granular soils. *Powders and grains*, 97: 169-183.

Lee, C., Shin, H., Lee, J.S. (2014). Behavior of sand–rubber particle mixtures: experimental observations and numerical simulations. *International Journal for Numerical and Analytical Methods in Geomechanics*, 38(16): 1651-1663. https://doi.org/10.1002/nag.2264.

Li, X.S., Dafalias, Y.F., Wang, Z.L. (1999). State-dependent dilatancy in critical-state constitutive modelling of sand. *Canadian Geotechnical Journal*, 36(4): 599-611. https://doi.org/10.1139/t99-029.

Liu M D, Carter J P. (2002). A structured Cam Clay model. *Canadian Geotechnical Journal*, 2002, 39(6): 1313-1332. https://doi.org/ 10.1139/t02-069.

Machado, S.L., Vilar, O.M., Carvalho, M.D.F. (2008). Constitutive model for long term municipal solid waste mechanical behavior. *Computers and Geotechnics*, 35(5): 775-790. https://doi.org/10.1016/j.compgeo.2007.11.008.

Mashiri, M.S., Vinod, J.S., Sheikh, M.N. (2016). Constitutive model for sand–tire chip mixture. *International Journal of Geomechanics*, 16(1): 04015022. https://doi.org/10.1061/(ASCE)GM.1943-5622.0000472.

Qi, Y., Indraratna, B., Heitor, A., Vinod, J.S. (2018). Effect of rubber crumbs on the cyclic behavior of steel furnace slag and coal wash mixtures. *Journal of Geotechnical and Geoenvironmental Engineering*, 144(2): 04017107. https://doi.org/10.1061/(asce)gt.1943-5606.0001827.

Saberian, M., Li, J., Kilmartin-Lynch, S., Boroujeni, M. (2021). Repurposing of COVID-19 single-use face masks for pavements base/subbase. *Science of the Total Environment*, 769: 145527. https://doi.org/10.1016/j.scitotenv.2021.145527.

Tang, C.S., Paleologos, E.K., Vitone, C., Du, Y.J., Li, J.S., Jiang, N.J., ... Singh, D.N. (2020). Environmental geotechnics: challenges and opportunities in the post-COVID-19 world. *Environmental Geotechnics*, 8(3): 172-192. https://doi.org/10.1680/jenge.20.00054.

ur Rehman, Z., Khalid, U. (2021). Reuse of COVID-19 face mask for the amelioration of mechanical properties of fat clay: A novel solution to an emerging waste problem. *Science of The Total Environment*, 794: 148746. https://doi.org/10.1016/j.scitotenv.2021.148746.

Wang, G., Li, J., Saberian, M., Rahat, M.H.H., Massarra, C., Buckhalter, C., Farrington, J., Collins, T., Johnson, J. (2022). Use of COVID-19 single-use face masks to improve the rutting resistance of asphalt pavement. *Science of the Total Environment*, 826: 154118. https://doi.org/10.1016/j.scitotenv.2022.154118.

Xu, W.Q., Yin, Z.Y., Wang, H.L., Wang, X. (2022). Experimental study on the monotonic mechanical behavior of completely decomposed granite soil reinforced by disposable face-mask chips. *Journal of Cleaner Production*, 352: 131528. https://doi.org/10.1016/j.jclepro.2022.131528.

Yin, Z.Y. (2021). Constitutive theory of granular soils and application. Beijing: China Architecture & Building Press.

Yin, Z.Y., Hicher, P.Y., Dano, C., Jin, Y.F. (2016). Modeling mechanical behavior of very coarse granular materials. *Journal of Engineering Mechanics*, 143(1): C4016006. https://doi.org/10.1061/(ASCE)EM.1943-7889.0001059.

Yin, Z.Y., Wu, Z.X., Hicher, P.Y. (2018). Modeling monotonic and cyclic behavior of granular materials by exponential constitutive function. *Journal of Engineering Mechanics*, 144(4): 04018014. https://doi.org/10.1061/(ASCE)EM.1943-7889.0001437.

Zaimoglu, A.S., Yetimoglu, T. (2012). Strength behavior of fine-grained soil reinforced with randomly distributed polypropylene fibers. *Geotechnical and Geological Engineering*, 30: 197-203. https://doi.org/10.1007/s10706-011-9462-5.

Zand, A.D., Heir, A.V. (2020). Emerging challenges in urban waste management in Tehran, Iran during the COVID-19 pandemic. *Resources, Conservation, and Recycling*, 162: 105051. https://doi.org/10.1016/j.resconrec.2020.105051.

Zhang, J.Q., Wang, X., Yin, Z.Y., Yang, N. (2022). Static and dynamic behaviors of granular soil reinforced by disposable face-mask chips. *Journal of Cleaner Production*, 331: 129838. https://doi.org/10.1016/j.jclepro.2021.129838.

Ciotti, M., et al. (2020). "The COVID-19 pandemic." Critical reviews in clinical laboratory sciences **57**(6): 365-388.

Haleem, A., et al. (2020). "Effects of COVID-19 pandemic in daily life." Current medicine research and practice 10(2): 78.

Betsch, C., et al. (2020). "Social and behavioral consequences of mask policies during the COVID-19 pandemic." Proceedings of the National Academy of Sciences **117**(36): 21851-21853.

Li, T., et al. (2020). "Mask or no mask for COVID-19: A public health and market study." Plos one **15**(8): e0237691.

Tirupathi, R., et al. (2020). "Comprehensive review of mask utility and challenges during the COVID-19 pandemic." Infez Med **28**(suppl 1): 57-63.

Pourebrahimi, S. (2022). "Upcycling face mask wastes generated during COVID-19 into value-added engineering materials: A review." Science of the Total Environment **851**: 158396.

Scheid, J. L., et al. (2020). "Commentary: physiological and psychological impact of face mask usage during the COVID-19 pandemic." International journal of environmental research and public health **17**(18): 6655.

Shetty, S. S., et al. (2020). "Discarded Covid 19 gear: A looming threat." Oral Oncology **107**: 104868.